Cell

Article

Posttranslational Modifications Mediate the Structural Diversity of Tauopathy Strains

Graphical Abstract

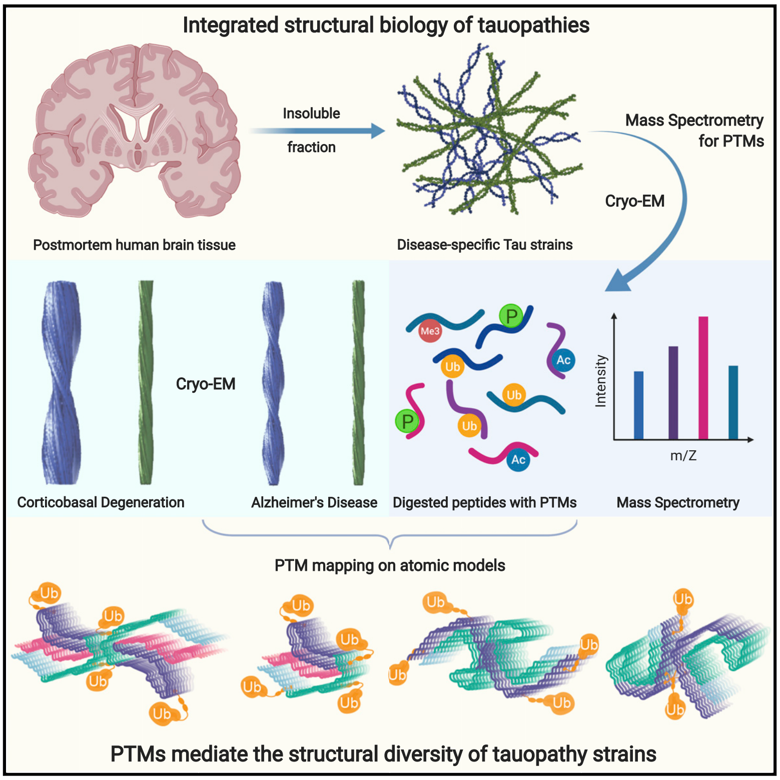

Highlights

- Cryo-EM structures of human brain-derived tau filaments from a four-repeat tauopathy
- Cryo-EM and MS of tau filaments enable PTM mapping directly onto atomic models
- Comparing tauopathies reveals that ubiquitination of tau can mediate fibril diversity
- Integrated structural biology elucidates principles of PTM-mediated fibril assembly

Authors

Tamta Arakhamia, Christina E. Lee,
Yari Carlomagno, ..., Nicholas T. Seyfried,
Leonard Petrucelli,
Anthony W.P. Fitzpatrick

Correspondence

petrucelli.leonard@mayo.edu (L.P.),
anthony.fitzpatrick@columbia.edu (A.W.P.F.)

In Brief

Structural and mass spectrometry-based proteomics of tau filaments, including their posttranslational modifications, from corticobasal degeneration and Alzheimer's disease point to how cross-talk between posttranslational modifications influences fibril structure, contributing to the structural diversity of tauopathy strains.

Arakhamia et al., 2020, Cell *180*, 633–644
February 20, 2020 © 2020 Elsevier Inc.
https://doi.org/10.1016/j.cell.2020.01.027

Cell

Posttranslational Modifications Mediate the Structural Diversity of Tauopathy Strains

Tamta Arakhamia,[1,2,3,8] Christina E. Lee,[1,2,3,8] Yari Carlomagno,[4,8] Duc M. Duong,[5] Sean R. Kundinger,[5] Kevin Wang,[1,2,3]
Dewight Williams,[7] Michael DeTure,[4] Dennis W. Dickson,[4] Casey N. Cook,[4] Nicholas T. Seyfried,[5,6] Leonard Petrucelli,[4,*]
and Anthony W.P. Fitzpatrick[1,2,3,9,*]
[1]Mortimer B. Zuckerman Mind Brain Behavior Institute, Columbia University, New York, NY 10027, USA
[2]Department of Biochemistry and Molecular Biophysics, Columbia University, New York, NY 10032, USA
[3]Taub Institute for Research on Alzheimer's Disease and the Aging Brain, Columbia University Irving Medical Center, New York, NY 10032, USA
[4]Department of Neuroscience, Mayo Clinic, Jacksonville, FL 32224, USA
[5]Department of Biochemistry, Emory University School of Medicine, Atlanta, GA 30322, USA
[6]Department of Neurology, Emory University School of Medicine, Atlanta, GA 30322, USA
[7]John M. Cowley Center for High Resolution Electron Microscopy, Arizona State University, Tempe, AZ 85287, USA
[8]These authors contributed equally
[9]Lead Contact
*Correspondence: petrucelli.leonard@mayo.edu (L.P.), anthony.fitzpatrick@columbia.edu (A.W.P.F.)
https://doi.org/10.1016/j.cell.2020.01.027

SUMMARY

Tau aggregation into insoluble filaments is the defining pathological hallmark of tauopathies. However, it is not known what controls the formation and templated seeding of strain-specific structures associated with individual tauopathies. Here, we use cryo-electron microscopy (cryo-EM) to determine the structures of tau filaments from corticobasal degeneration (CBD) human brain tissue. Cryo-EM and mass spectrometry of tau filaments from CBD reveal that this conformer is heavily decorated with posttranslational modifications (PTMs), enabling us to map PTMs directly onto the structures. By comparing the structures and PTMs of tau filaments from CBD and Alzheimer's disease, it is found that ubiquitination of tau can mediate interprotofilament interfaces. We propose a structure-based model in which cross-talk between PTMs influences tau filament structure, contributing to the structural diversity of tauopathy strains. Our approach establishes a framework for further elucidating the relationship between the structures of polymorphic fibrils, including their PTMs, and neurodegenerative disease.

INTRODUCTION

Tauopathies are a broad class of neurodegenerative diseases characterized by pathological aggregation of the tau protein (Ballatore et al., 2007). These diseases present diverse clinical syndromes with substantial variability in phenotype within affected families and between patients (Irwin, 2016). Primary tauopathies, such as Pick's disease (PiD) and corticobasal degeneration (CBD), are epitomized by neuronal and glial tau inclusions (Dickson et al., 2011), whereas Alzheimer's disease (AD), a secondary tauopathy, is typified by a combination of tau aggregates and extracellular amyloid plaques (Bloom, 2014). Little is known about how abnormal tau can give rise to such varied phenotypes, but recent structures have identified differently folded forms of tau forming the building block of the amyloid state (Eisenberg and Jucker, 2012) in different tauopathies (Falcon et al., 2018a, 2019; Fitzpatrick et al., 2017). These results have led to the hypothesis that each tauopathy may be characterized by a disease-specific, misfolded conformer (Fitzpatrick and Saibil, 2019; Goedert et al., 2018).

At the molecular level, misfolded tau aggregates via distinct conformations (or strains) of the monomer, which are likely to be influenced by the local cellular environment (Kaufman et al., 2016). These form hydrogen-bonded protofilaments, which may pack together laterally into fibrils in multiple ways (Fitzpatrick et al., 2017). This hierarchical assembly leads to molecular (Petkova et al., 2005) and ultrastructural polymorphism (Fitzpatrick et al., 2013; Fitzpatrick and Saibil, 2019), giving rise to unique molecular signatures for each tauopathy (Falcon et al., 2018a, 2019; Fitzpatrick et al., 2017). However, two key questions remain: why do misfolded tau molecules consistently aggregate into unique, disease-specific strains? And what are the tau and non-tau components directing this pathological self-assembly?

A potential explanation lies in posttranslational modification (PTM), the least understood molecular determinant of tauopathies (Kontaxi et al., 2017; Park et al., 2018). Numerous PTMs of tau have been identified (Mandelkow and Mandelkow, 2012), with differences in modification profiles detected in different tauopathies (Kontaxi et al., 2017; Park et al., 2018). We hypothesized that such changes, regulated or otherwise, to the amino-acid sequence could modulate the conformational state of the tau monomer and manifest themselves in the structure of tau filaments. However, structural studies have failed to identify PTMs (Falcon et al., 2018a, 2019; Fitzpatrick et al.,

2017) likely because of the treatment of the tau (Falcon et al., 2018a) and other tissue-derived (Kollmer et al., 2019) protein filaments with pronase to achieve high-resolution cryo-electron microscopy (cryo-EM) maps.

Here, using a combination of cryo-EM and mass spectrometry (MS)-based proteomics, we identified the insoluble filament core and solved the structures of posttranslationally modified straight and twisted tau filaments from the brains of patients with CBD (Ksiezak-Reding et al., 1996; Tracz et al., 1997) or AD (Crowther, 1991; Kidd, 1963; Terry, 1963). In this study, we imaged undigested tau filaments using cryo-EM in order to fully resolve tau protein conformers in CBD and AD, complete with the PTMs that form a crucial and biologically informative part of the structures. In addition to mapping PTMs from multiple cases onto atomic models of tau filaments from CBD and AD, we identified a structural role played by PTMs in mediating inter-protofilament interfaces. As such, we propose a structure-based model in which site-specific ubiquitination of tau influences the resulting filament structure, thereby modulating distinct fibril subpopulations.

RESULTS

Structures of Tau Filaments in CBD, a Four-Repeat Tauopathy

A distinctive neuropathologic feature of CBD is focal cortical atrophy with swollen cortical neurons (“ballooned neurons” [BN], Figure 1A), which contain phosphorylated neurofilaments (Dickson et al., 1986). In addition to BN, affected cortical and subcortical areas have many tau-immunoreactive neuronal processes (“threads,” Figures 1B–1D) and pleomorphic neuronal inclusions (Figures 1C and 1D). The latter may be densely packed inclusions reminiscent of Pick bodies or small neurofibrillary tangles (NFTs) or filamentous inclusions that are more dispersed and disorderly, consistent with so-called pretangles. Accompanying threads and pretangles are tau-positive argyrophilic inclusions in oligodendroglia (often referred to as “coiled bodies”) (Braak and Braak, 1998), as well as tau-immunoreactive astrocytic lesions that appear as annular clusters of short fuzzy cell processes, which may be suggestive of a neuritic plaque. These astrocytic lesions are referred to as “astrocytic plaques” (Feany and Dickson, 1995). Tau lesions in CBD are composed predominantly of tau isoforms containing four microtubule-binding repeats (4R tau) (Sergeant et al., 1999), with ultrastructural studies revealing both straight and twisted filaments (Ksiezak-Reding et al., 1996; Tracz et al., 1997).

Sarkosyl-insoluble material used for cryo-EM was first evaluated by western blot (Figure 1E), immunogold negative stain

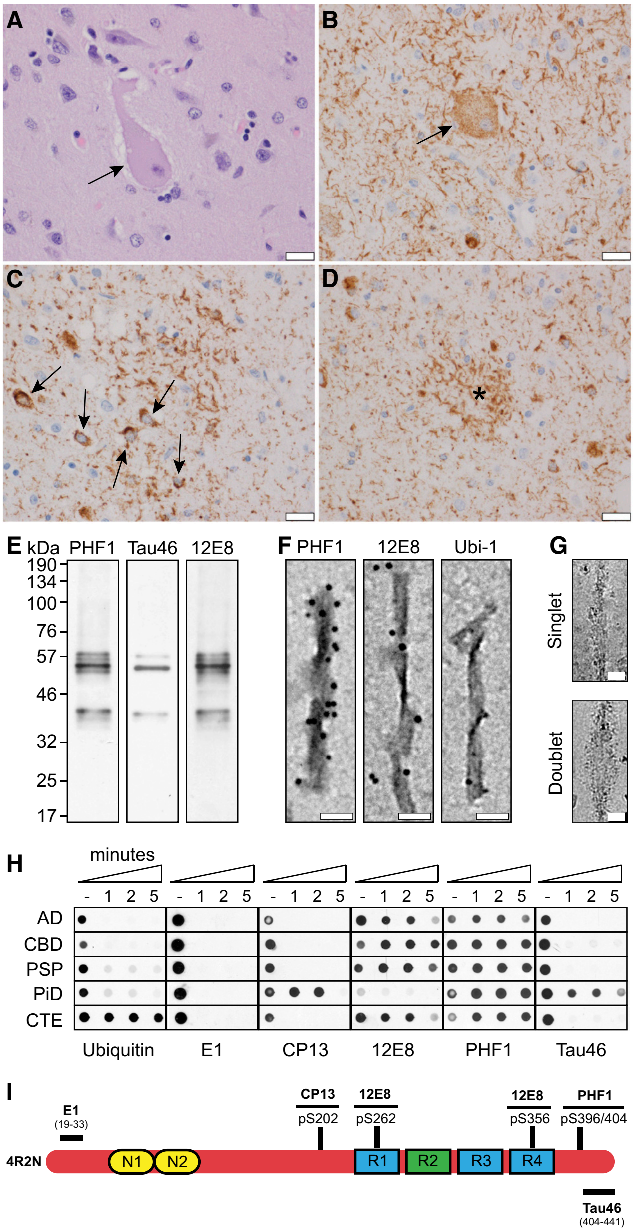

Figure 1. Neuropathological and Biochemical Characterization of CBD Tau Filaments

(A–D) Representative neuropathological changes in the frontal cortex of a patient with CBD. Ballooned neurons revealed by H&E staining (A, arrow) and immunolabeling with CP13 (B, arrow). CP13 immunostaining also labels neuritic threads (B–D), as well as pleomorphic small neuronal inclusions (C, arrows) and astrocytic plaques (D, asterisk). Scale bar: 20 μm (A–D).

(E) Sarkosyl-insoluble material from the frontal cortex of the CBD patient used for cryo-EM and MS analysis was evaluated by western blot, using the tau antibodies PHF1 (pS396/404), Tau46 (aa404-441), and 12E8 (pS262, pS356).

(F) Representative immuno-electron microscopy images of sarkosyl-insoluble tau filaments purified from CBD brain and stained with tau phospho-specific antibodies PHF1 and 12E8, as well as ubiquitin (Ubi-1). Primary antibodies were visualized with secondary antibody conjugated with 6 nm gold particles. Scale bar: 30 nm.

(G) Representative cryo-EM images of the singlet and doublet tau fibrils in CBD. Scale bar: 100 Å.

(H) Pronase treatment eliminates Ubi-1 immunoreactivity from sarkosyl-insoluble core. To examine the impact of pronase treatment on ubiquitination of the filament core in tauopathies, the sarkosyl-insoluble fraction was obtained and incubated in the presence or absence of pronase (1, 2, or 5 min treatment) and subsequently evaluated by dot blot (using anti-Ubi-1 and the tau antibodies E1 [aa19-33], CP13 [pS202], 12E8, PHF1, and Tau46). Note that the amount of each sarkosyl-insoluble fraction was normalized for total tau levels.

(I) Schematic diagram depicting the location of each antibody epitope within the tau protein.

See also Figures S1 and S5.

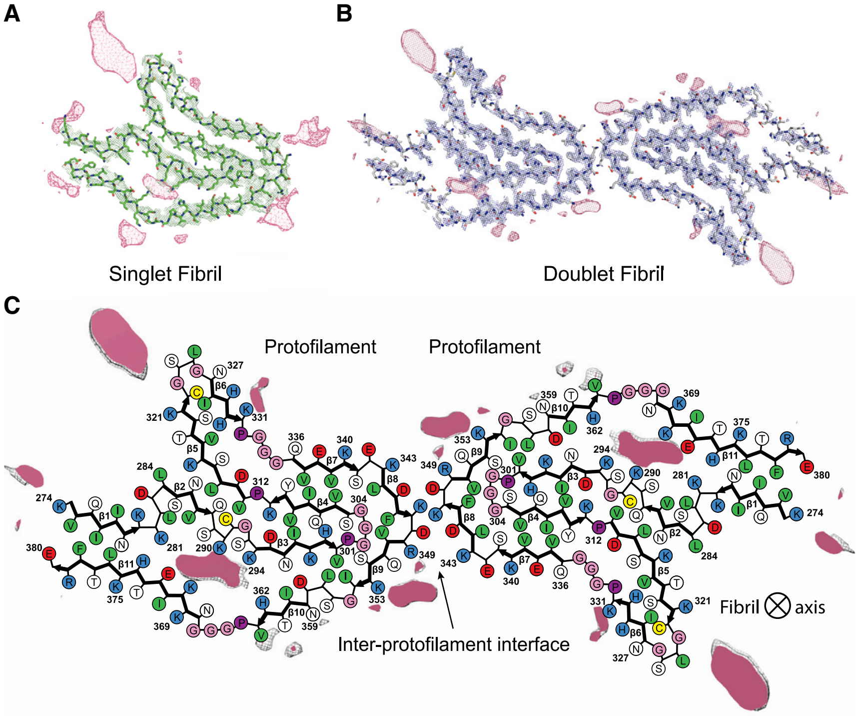

Figure 2. Cryo-EM Structures of Tau Filaments from CBD

(A and B) Cryo-EM density (mesh) and atomic models (colored sticks) of (A) singlet and (B) doublet fibrils in CBD. Extra densities (pink mesh), which are directly connected or in close proximity to many sidechains in the cryo-EM maps, correspond to non-tau protein components.

(C) Schematic view of the CBD doublet fibril. The extra, unknown densities are overlaid as capped pink mesh.

See also Figure S2.

EM (Figure 1F), cryo-EM (Figure 1G), and pronase-resistance by dot blot analysis (Figure 1H). In particular, immunoreactivity of various tau antibodies (Ercan et al., 2017; Irwin et al., 2012; Morris et al., 2015) (Figure 1I) was utilized to confirm that pronase treatment effectively removed soluble regions of the tau protein that were exposed while regions inside the filament core were protected and thus resistant to pronase activity. As anticipated, pronase treatment of CBD sarkosyl-insoluble material eliminated immunoreactivity of the extreme N- and C-terminal epitopes detected by E1 and Tau46, respectively. CP13 (pS202) was also sensitive to pronase, indicating that this phospho-epitope is outside of the filament core in CBD. Conversely, 12E8 (pS262/356) and PHF1 (pS396/404) were pronase-resistant, suggesting that CBD sarkosyl-insoluble material is phosphorylated at both epitopes and that these PTMs are not impacted by exposure to pronase. Similar results were observed with sarkosyl-insoluble material from AD and the tauopathies progressive supranuclear palsy and chronic traumatic encephalopathy (CTE), whereas notable differences in pronase sensitivity and resistance of tau epitopes were detected in sarkosyl-insoluble material from PiD. Finally, ubiquitination of sarkosyl-insoluble material was evaluated both prior to and following exposure to pronase. Although abundant ubiquitin immunoreactivity is observed in CBD sarkosyl-insoluble material, the signal quickly disappears upon pronase treatment, indicating that pronase eliminates ubiquitination of the CBD tau core. The sarkosyl-insoluble material from other tauopathies exhibited a similar sensitivity of ubiquitin immunoreactivity toward pronase with the exception of CTE. Given the loss of ubiquitination upon exposure to pronase, these results reveal that pronase treatment (Falcon et al., 2018a; Kollmer et al., 2019) will result in incomplete structure determination, particularly with respect to ubiquitination, so we proceeded without including this step.

Following basic characterization of the sarkosyl-insoluble material used for cryo-EM analysis (Figures 1A–1F and S1), we then examined filament morphology at high resolution. Consistent with previous reports (Ksiezak-Reding et al., 1996; Tracz et al., 1997), CBD sarkosyl-insoluble fractions were characterized by both twisted and straight filaments (readily distinguishable in cryo-EM images), with twisted filaments measuring twice the width of straight filaments (Figure 1G). We designated these two subtypes as doublet and singlet fibrils, respectively. Singlet fibrils have a helical twist with a crossover distance of approximately 1,050 Å, whereas doublet fibrils have a crossover distance of approximately 1,300 Å, with the ratio of singlet to doublet fibrils being approximately 1:2.

Singlet (Figure 2A) and doublet (Figure 2B) fibrils were manually selected and reconstructed from 30,804 micrographs, using helical reconstruction in RELION, to a resolution of 4.3 Å and 3.8 Å, respectively (Figure S2). Singlet fibrils are composed of a single protofilament (Figure 2A), whereas doublet fibrils exhibit a 2-fold symmetrical arrangement of this common protofilament (Figure 2B). Note that strong, large densities are visibly attached to K_{321}, K_{343}, K_{353}, H_{362}, and K_{369} on our singlet map (Figure 2A) and K_{321}, K_{353}, and H_{362} on our doublet map (Figure 2B), indicating that non-tau components are an integral part of the CBD tau fibril core (Figure 2C).

The core structure is comprised of residues K_{274}–E_{380} of the tau protein, spanning the last residue of R1, all of R2–R4, and 12 amino acids following R4 (Figure 3A). This tau fold adopts 11 β strands (β1–β11): three from R2 (β1–β3), three from R3 (β4–β6), four from R4 (β7–β10), and one formed by N_{368}–E_{380} (β11) (Figure 2C). The β strands are interconnected by β-breaking prolines (P_{312}), β-turn glycines (G_{292}, G_{323}), or β-arc residues (D_{283}, E_{342}, D_{348}) (Figures 2C and 3A). The tandem repeats R1–R4 all contain a versatile PGGG motif that can form a tight turn between β3 → β4 or adopt an extended β-spiral conformation connecting β6 → β7 and β10 → β11 (Figures 2C and 3A). Multi-sheet, cross-β interfaces are formed between β10 → β3 → β4 → β7 and β6 → β5 → β2 (Figure 2). The N and C termini close the common protofilament structure by packing β1 against

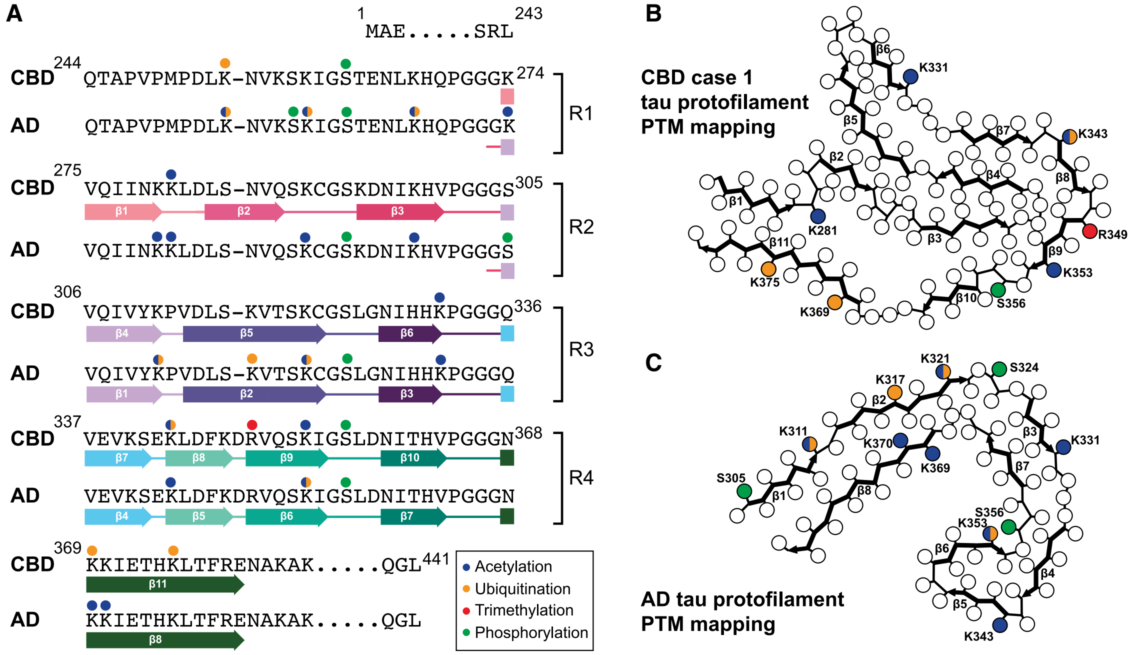

Figure 3. PTMs of Tau Filaments from CBD and AD Detected by MS

(A) Sequence alignment of the four microtubule-binding repeats (R1–R4) of tau and the sequence after R4 that are part of the CBD and AD fibril cores. The positions of filamentous β strands in both diseases are shown. PTMs detected by MS in tau fibrils from CBD case 1 and AD, the structures of which were determined by cryo-EM in this work, are shown with acetylation, ubiquitination, trimethylation, and phosphorylation sites marked with blue, orange, red, and green balls, respectively. Sidechains with multiple PTMs detected are shown with two colors. Acetylation of K_{321} and K_{370} (Park et al., 2018) and ubiquitination of K_{353} (Cripps et al., 2006) in the AD fibril core are included from the literature.

(B and C) PTMs are mapped onto schematics of the protofilament structures from (B) CBD case 1, and (C) AD. The same color scheme as described above is used to depict PTMs.

See also Figures S4 and S7and Tables S1, S2, S3, and S4.

β11 (Figure 2). Clustering different combinations of the hydrophobic residues F, I, L, and V stabilizes most of the inter-sheet interfaces (Figure 2C). Notably, a large, rhomboidal, and hydrophilic cavity is formed by residues K_{281}–N_{296} and D_{358}–H_{374}, which enclose an unknown, organic density that is not part of the tau molecule (Figure 2).

Comparison of CBD and AD Tau Filament Structures

Similar to other tau conformers (Falcon et al., 2018a, 2019; Fitzpatrick et al., 2017), an ordered, in-register, and parallel hydrogen-bonding pattern is maintained throughout the disease-specific CBD tau protofilament structure. In terms of intra-sheet sidechain stacking and secondary structure, tau filaments from CBD closely match those from AD, with the main difference being that R2 and one C-terminal residue from R1 are in the ordered core structure (Figures 2C and 3). The β strand and loop-forming segments in CBD and AD are identical in one C-terminal residue from R1 or R2, all of R3 and R4, and 12 residues beyond R4 (Figure 3). This indicates that the tau molecule can misfold into myriad conformers while preserving highly conserved secondary structure motifs (Figure 3). The diversity of disease-specific protofilament structures becomes apparent when comparing inter-sheet interactions, which we visualize using contact maps (Figures 4A, 4B, and S3). By plotting a heatmap of inter-residue Cα-Cα distances within the tau protofilaments found in CBD (Figure 4A), AD (Figure 4B), and PiD (Figure S3), it is possible to clearly identify the inter-sheet contacts that nucleate and propagate these disease-specific strains. The CBD tau protofilament is shaped by close interactions between K_{369}–E_{380} → R2, R4 → R2, R2 → R3, and R3 → R3; the AD tau protofilament by R3 → R4 and K_{369}–E_{380} → R3 (the CTE tau protofilament is almost identical to AD) (Falcon et al., 2019; Fitzpatrick et al., 2017); and the PiD tau protofilament by K_{369}–E_{378} → R4, R1 → R4, and R3 → R3 (Falcon et al., 2018a). Overall, the aggregation of different tau isoforms—4R tau (CBD), 4R + 3R tau (AD and CTE), and 3R tau (PiD)—occurs by forming inter-sheet contacts between permutations of R1–R4 and K_{369}–E_{380}, leading to enormously different intra-protofilament packings and unique conformational strains (Falcon et al., 2018a, 2019; Fitzpatrick et al., 2017). What is emerging, however, is that each tauopathy has a characteristic strain, which is observed in multiple patients and different brain regions (Falcon et al., 2018b). Given that recombinant tau can misfold into many different conformers (Zhang et al., 2019a), this implies that there may be other factors modulating tau fibrillar self-assembly *in vivo* to faithfully nucleate and seed unique strains in each tauopathy.

Structural Role of PTMs in CBD and AD Tau Strains

Given the ordered cores of tau filaments in CBD and AD share almost all secondary structure elements apart from additional β

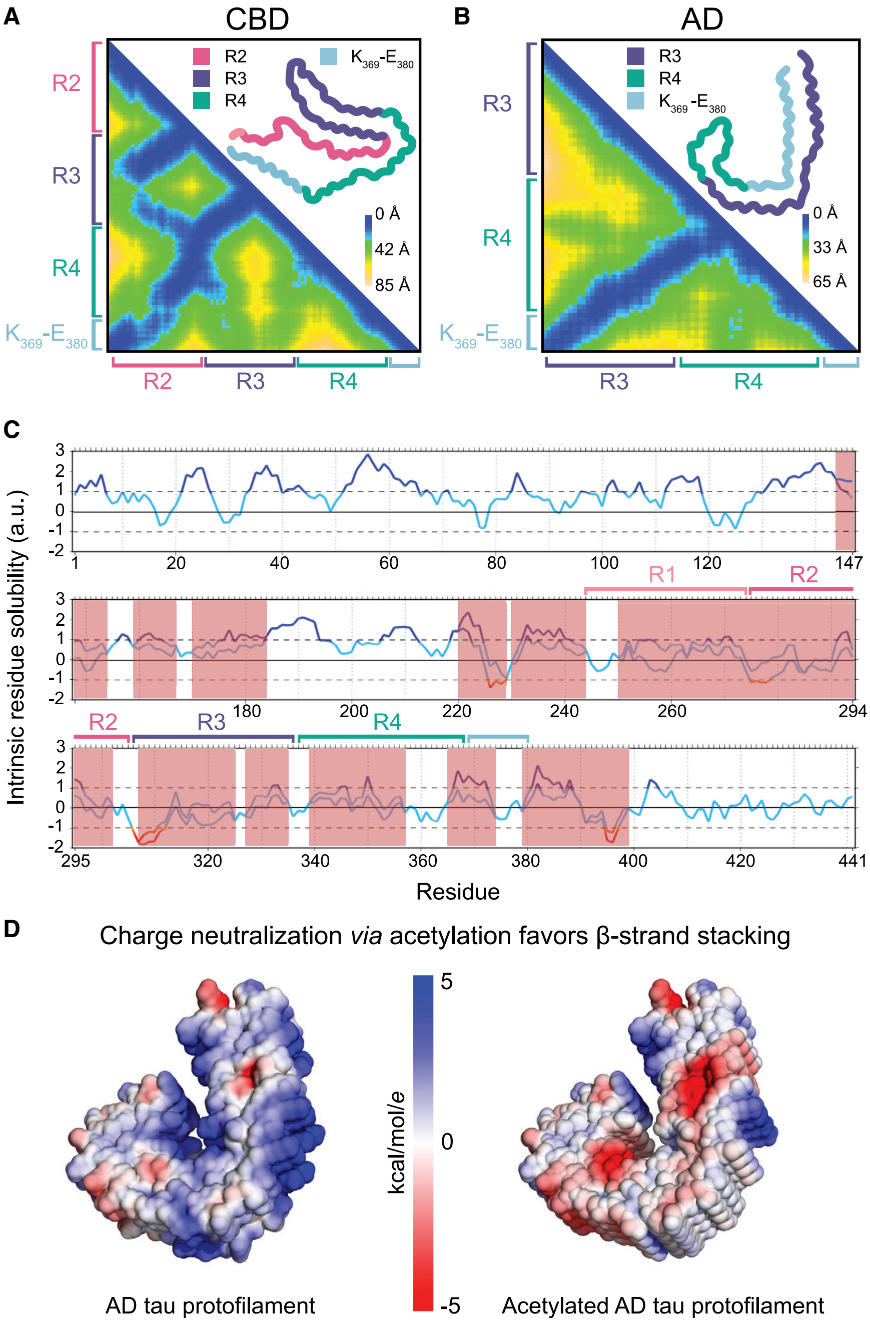

Figure 4. Intra-protofilament Contacts and Effect of Acetylation on the Fibril Core

(A and B) Heatmaps of inter-residue Cα-Cα distances within the tau protofilaments found in (A) CBD and (B) AD, indicating the interactions between microtubule binding repeats (R1–R4) and $K_{369–380}$ of tau.

(C) Predicted effects of acetylation, as represented by an acetyl-lysine mimic by mutating lysine (K) to glutamine (Q), on the solubility of the tau protein extracted from AD brain. Regions of altered residue solubility are highlighted in red, with positive values indicating soluble regions and negative values corresponding to aggregation-prone regions. Only acetylated residues implicated in AD brain (Park et al., 2018) were substituted.

(D) Surface representation of (left) unmodified tau protofilament from AD and (right) acetylated tau colored by electrostatic potential.

See also Figure S3.

strands formed by R2 in CBD, we used MS (Figures 3 and S4; Tables S1, S2, S3, and S4) to identify the additional densities connected to tau filaments in CBD (Figure 2) and AD (Fitzpatrick et al., 2017; Goedert et al., 2018), which we hypothesized could be PTMs. We performed MS on tau filaments from CBD case 1 (Figure 1), the structures of which were solved by cryo-EM (Figure 2); CBD case 2 (Figures S5A–S5C); two small pooled CBD cohorts (Table S1); and a single AD case (Figures S5D–S5I), which was also solved by cryo-EM (Figures S2D and S6). In the fibril-forming core regions of tau filaments from CBD (K_{274}–E_{380}) and AD (G_{304}–E_{380}), we achieved 96% and 100% sequence coverage, respectively (Figure 3; Tables S1 and S2). Tau filaments in CBD and AD have extensive PTMs, including phosphorylation, trimethylation, acetylation, and ubiquitination (Figures 3 and S4). Phosphorylation occurs largely in the fuzzy coat (Figure S4), with the tandem repeats R1–R4 and K_{369}–E_{380} almost exclusively acetylated or ubiquitinated (Figure 3). Although we cannot completely exclude modifications by ubiquitin-like proteins such as SUMOylation (Luo et al., 2014) or Neddylation (Dil Kuazi et al., 2003), MS analysis of polyubiquitinated tau in sarkosyl-insoluble fractions from CBD and AD postmortem tissue yielded orders of magnitude more spectral counts of C-terminal $_{76}GG_{75}$ ubiquitin fragments and ubiquitin sites (Tables S1, S2, and S4) than these rare PTMs.

The majority of acetylation or ubiquitination sites occur within the fibril-forming core regions in CBD (Figures 3B and S7) and AD (Figure 3C), suggesting that these modifications may play a role in modulating pathological tau aggregation. By neutralizing the repulsion of positively charged lysine residues, acetylation in a site-specific manner is predicted to make the tau protein less soluble (Figure 4C) and has been shown to promote tau aggregation (Cohen et al., 2011; Trzeciakiewicz et al., 2017) and to inhibit pathological tau degradation (Min et al., 2010). Charge neutralization of lysines via acetylation makes parallel, in-register stacking of β strands more favorable, because there is less charge repulsion between positively charged sidechains (Figure 4D).

Ubiquitination of tau filaments in CBD and AD may not only be a signal for degradation (Myeku et al., 2016; Petrucelli et al.,

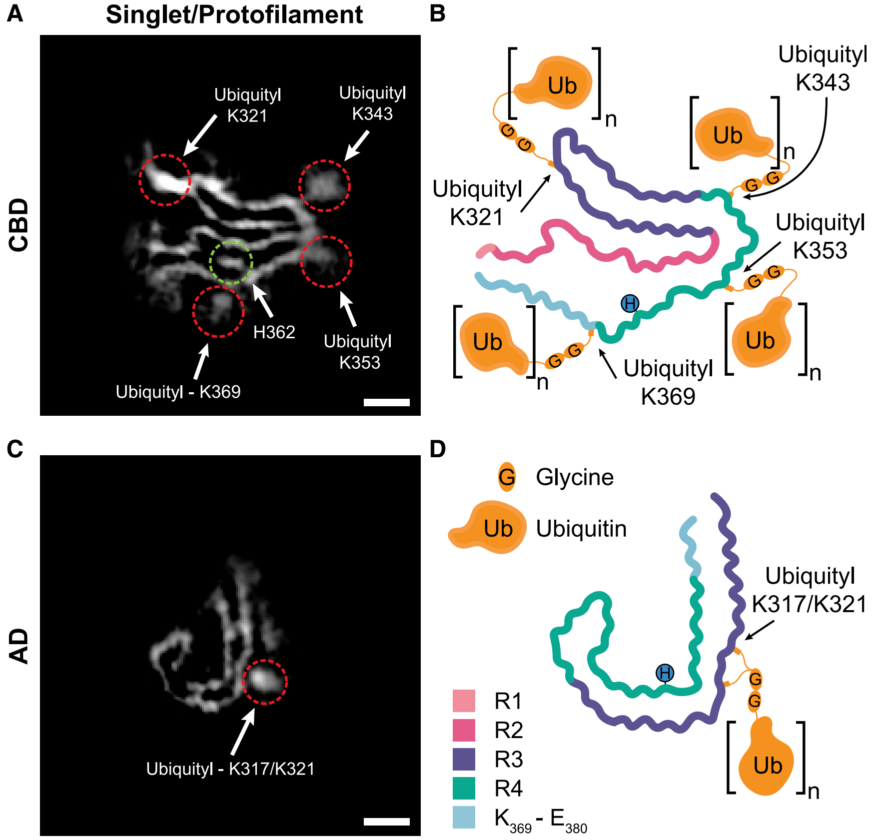

Figure 5. Visualization of PTMs of Tau Protofilaments from CBD and AD Using a Combination of Cryo-EM and MS PTM Mapping

Averages of 10 z-slices from the (A) CBD singlet fibril and (C) AD tau fibril cryo-EM 3D reconstructions reveal strong, large densities visibly attached to K_{321}, K_{343}, K_{353}, and K_{369} on the CBD singlet map and K_{317} and K_{321} on the AD tau protofilament (red dashed circles). Many of these sites are detected to be ubiquitinated by MS, and the lysine-connected densities are much too large to be an acetyl group. A large, buried density proximal to K_{290}, K_{294}, H_{362}, and K_{370} in the CBD singlet fibril is also shown (green dashed circle). Schematics shown to scale in (B) and (D) highlight the structural role that mono- or poly-ubiquitinated chains at these lysines may play in the CBD singlet fibril and AD tau protofilament, respectively. Brackets surrounding ubiquitin indicate the possibility of a (poly)-ubiquitin chain. The position of the H_{362} sidechain is shown as a filled blue circle. Scale bar: 25 Å.

2004) but could also play a structural role in fibrillization (Dickey et al., 2006; Park et al., 2018). MS indicates that tau filaments in CBD have three ubiquitination sites per protofilament at K_{343}, K_{369}, and K_{375} (Figures 3B and S7). Strong, large densities are visibly attached to K_{321}, K_{343}, K_{353}, and K_{369} on our singlet map (Figure 5A) and K_{321} and K_{353} on our doublet map (Figure 6A), indicating additional proteinaceous material at the periphery of the fibril core. The tau protofilaments in AD also display additional densities connected to lysine sidechains, which are particularly visible at K_{317} and K_{321} (Figures 5C, 6C and S6). MS of tau filaments in AD (Figures 3A and 3C) indicates that K_{311}, K_{317}, and K_{321} are ubiquitinated, consistent with previous reports (Abreha et al., 2018; Cripps et al., 2006; Park et al., 2018).

Based on a combination of MS and strong, large lysine-connected cryo-EM densities, we propose that the tau protofilaments in AD and CBD are mono- or poly-ubiquitinated (Abreha et al., 2018; Cripps et al., 2006). The terminal $_{76}GG_{75}$ ubiquitin fragment density is as strong as that of tau (Figures 5A and 5C), suggesting near-stoichiometric occupancy, with the rest of the ubiquitin molecules either cleaved or highly dynamic and thus not visible by cryo-EM helical reconstruction. In addition to marking the fibril for degradation by the 20S and 26S proteasome (Lee et al., 2013), stacking of ubiquitin chains covalently attached to the protofilament subunits in CBD (Figure 5B) and AD (Figure 5D) may stabilize the β strand stacking along the long axis of the fibrils.

In CBD doublet fibrils, the packing between protofilaments is mediated by antiparallel stacking of $_{343}KLDFKDR_{349}$ through (1) van der Waals interactions between K_{347} sidechains from each protofilament and (2) two pairs of hydrogen bonds between the ε-amino group of K_{347} and the carboxyl group of D_{348} and the backbone carbonyl of K_{347} on the opposite protofilament (Figure 2B). This interface may be additionally stabilized by ubiquitination of K_{353} (Figures 2B and 2C), because there is strong, large density in this region that may represent the C terminus of (mono/poly)-ubiquitin chains (Figure 6A). Much like the CBD singlet fibril, the doublet fibril shows strong, large extra densities connected to K_{321} and K_{353}, which can accommodate a terminal $_{76}GG_{75}$ ubiquitin fragment. Interestingly, there is no additional density connected to K_{343} (Figure 6A) in the doublet map, suggesting that these sites may not be highly ubiquitinated in this ultrastructural polymorph (Figure 6B).

In comparison, the asymmetric packing of the straight filament formed by tau in AD (Falcon et al., 2018b; Fitzpatrick et al., 2017) is mediated by a region of additional density that is connected to the $K_{317/321}$ lysine side chains on both protofilaments (Figure 6C). The nature of this stabilizing interaction was previously unknown, and it has been postulated that this density may be composed of $_{7}EFE_{9}$ because it interacts with K_{317} and $K_{321,}$ potentially forming salt bridges that link the distal end of the N terminus with the filament core (Fitzpatrick et al., 2017; Goedert et al., 2018). On the other hand, it has been demonstrated that an extended $_{7}EFE_{9}$ structure cannot fit into this inter-protofilament interface without causing steric clashes (Boyer and Eisenberg, 2019). Based on our MS findings, we are able to build a C-terminal $_{76}GG_{75}$ ubiquitin fragment covalently attached to the ε-NH_2 group of K_{317} via an isopeptide bond into this previously unknown density (Figure S6). This atomic model implies that the binding interface between protofilaments in AD straight filaments may be

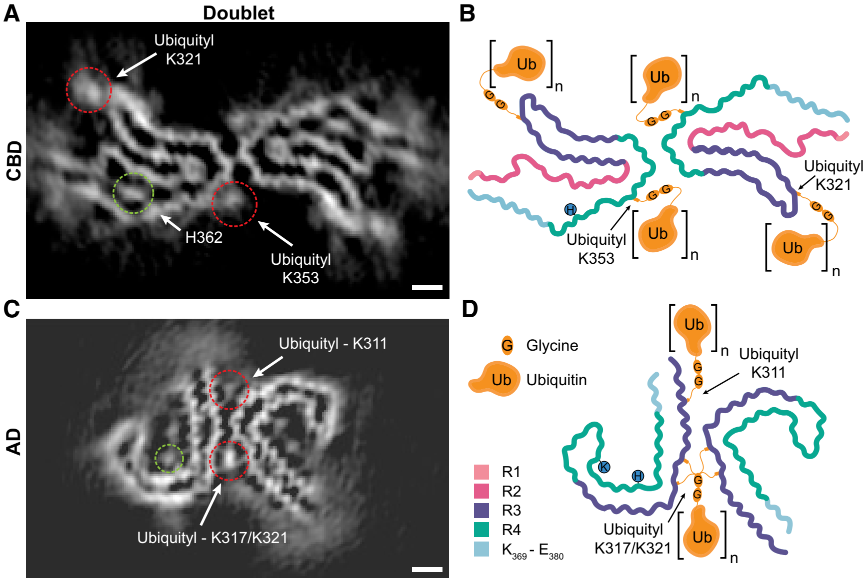

Figure 6. Visualization of PTMs of Tau Fibrils from CBD and AD Using a Combination of Cryo-EM and MS PTM Mapping

Averages of 10 z-slices from the (A) CBD doublet fibril and (C) AD straight filament (EMD-3743) cryo-EM 3D reconstructions reveal strong, large densities visibly attached to K_{321} and K_{353} on the CBD doublet map and K_{311}, K_{317}, and K_{321} on the AD straight filament (red dashed circles). In particular, note the large, near-stoichiometric densities at the interface between protofilaments (A and C). Many of these sites are detected to be ubiquitinated by MS, and the lysine-connected densities are much too large to be an acetyl group. A large, buried density proximal to K_{290}, K_{294}, H_{362}, and K_{370} in the CBD doublet fibril and a large, solvent-exposed density next to K_{353}, H_{362}, and K_{369} in the AD straight filament are also shown (green dashed circle). Schematics shown to scale in (B) and (D) highlight the structural role that mono- or poly-ubiquitinated chains at these lysines may play in the CBD doublet fibril and AD straight filament, respectively. Brackets surrounding ubiquitin indicate the possibility of a (poly)-ubiquitin chain. The position of the K_{353} and H_{362} sidechains are shown as filled blue circles. Scale bar: 25 Å.

See also Figure S6.

stabilized by additional interactions with the C terminus of the ubiquitin chain.

DISCUSSION

By comparing the structures of posttranslationally modified tau filaments in CBD and AD, we identify many common structural elements (Figure 3) as well as both shared and distinct PTMs (Figure S4; Tables S1 and S2). The picture that emerges is that the β strand-forming motifs in the two diseases are highly similar, but their misfolding and self-assembly into fibrils is radically different (Figures 4A and 4B). This diversity is facilitated by the loops and turns adopted by glycine and proline residues, which can accommodate myriad inter-sheet packings of the β strand building blocks. The unusually high percentage of glycine residues in the fibril-forming cores in CBD (12.1%) and AD (13.0%) points to their critical role in allowing β strands to flex and turn. Each tau repeat contains a PGGG motif that can adopt a compact turn or an extended conformation (Figures 2 and 3) (Fitzpatrick et al., 2017), enabling the tandem repeats R1–R4 to adopt an almost continuous β strand architecture. Valine makes up over 10% of the fibril cores in CBD and AD, and together with isoleucine, leucine, and phenylalanine, these hydrophobic residues (FILV) stabilize most of the inter-sheet interfaces through clustering, aliphatic stacking, and aromatic stacking. Distinct FILV clusters can be identified in CBD and AD fibril cores (Fitzpatrick et al., 2017), cementing the closest sheet-sheet interactions between β strands (Figure 2C). The inclusion of R2 in the CBD tau fibril core radically alters inter-β sheet contacts (Figures 4A, 4B, and S3), resulting in a strain distinct from other tauopathies (Falcon et al., 2018a, 2019; Fitzpatrick et al., 2017).

The singlet and doublet fibrils formed by tau in CBD contain a small molecule buried within a large, hydrophilic cavity that may stabilize the CBD fold during fibril nucleation and/or templated seeding. The cavity is defined by three lysines (K_{290}, K_{294}, K_{370}) and a buried histidine (H_{362}), all pointing toward this additional, organic density (Figure 2). To charge-compensate the spatially proximal lysine sidechains, this density may represent a small molecule with a net charge of −3 per rung of the protofilament. The size of the negatively charged small molecule is approximately 9 Å × 4 Å (Figures 2, 5A, and 6A), with near-stoichiometric occupancy so that it corresponds to a minimum volume of 170 $Å^3$. Assuming an average density of organic compounds to be 1 g/cm^3, the unknown molecule has an estimated molecular weight with a lower bound of 100 Da (or roughly the average size of an amino acid).

Although it was not possible to identify this small molecule using cryo-EM or MS, it appears to be most strongly connected to H_{362} (Figures 2A, 2B, and 5A). Solvent-exposed extra densities conjugated to the H_{362} sidechain appear in cryo-EM maps of tau filaments in AD (Figure 6C) and CTE (Falcon et al., 2019), but not in PiD (Falcon et al., 2018a), whereas in CBD, this additional density is buried within the core of the filament, forming part of the internal structure (Figures 2, 5A, and 6A). We do not see phosphorylation or methylation of H_{362} in tau filaments from CBD or AD by MS (Figure 3). However, given that there appears to be a large, negatively charged molecule conjugated to H_{362} in tau filaments from CBD (Figures 2, 5A, and 6A), it is possible that this density corresponds to an ADP-ribose moiety or N-linked glycan. It is important to note that poly(ADP-ribose) drives pathological aggregation of α-synuclein, accelerating fibrillization and converting it into a more toxic α-synuclein strain (Kam et al., 2018). Also, tau is N-glycosylated in AD brain, but not in healthy brain (Wang et al., 1996), and studies have shown not only that glycans modulate tau aggregation (Losev et al., 2019) but also that deglycosylation alters tau paired helical

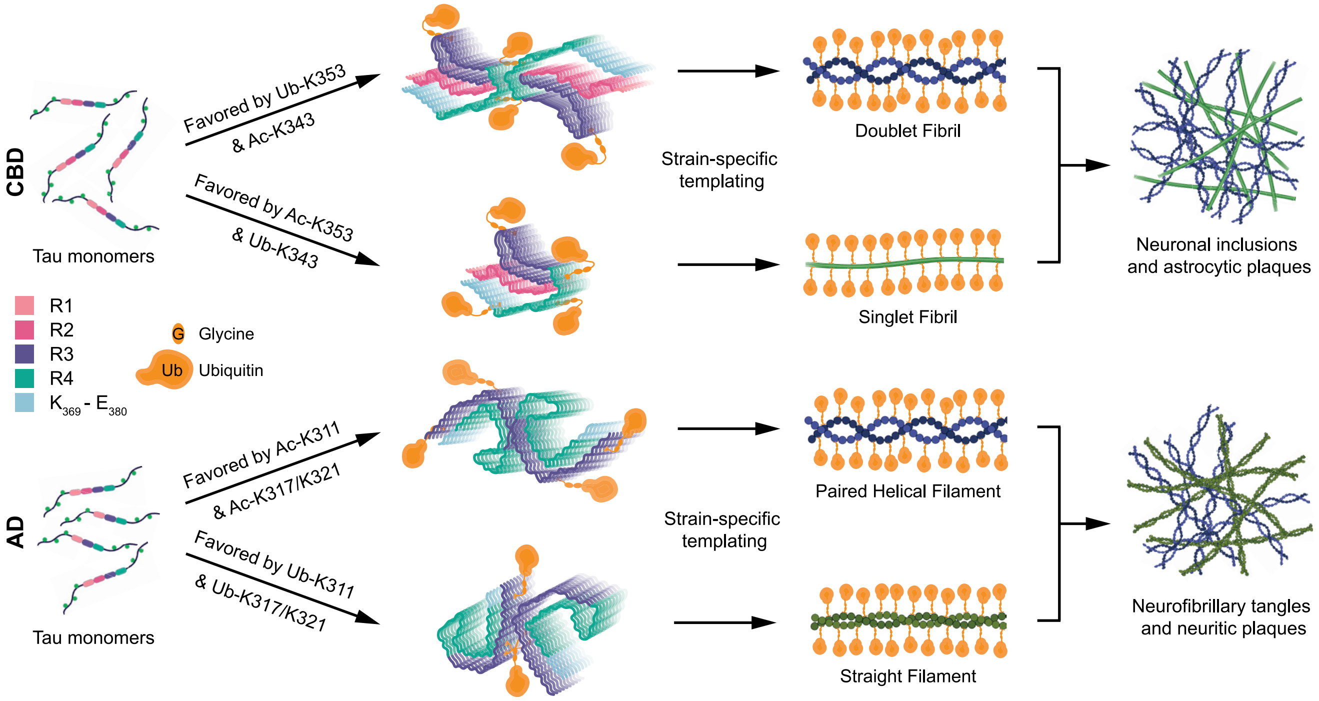

Figure 7. Proposed Structure-Based Model of How Interplay between PTMs Influences Tau Filament Structure

Based on our cryo-EM maps and MS PTM mapping onto atomic models, we conclude that ubiquitination of tau can mediate inter-protofilament interfaces in the doublet CBD fibril and straight filament from AD. If sites on tau favoring the formation of doublet fibrils in CBD (K_{353}) or straight filaments in AD (K_{311} and $K_{317/321}$) are acetylated, or ubiquitinated with low occupancy, this inter-protofilament interface is less likely to form. The singlet fibril in CBD does not bind to a second protofilament, and paired helical filaments in AD have structures that do not require mediation by non-tau components at their inter-protofilament interface. The outcome of this model is that the incorporation of ubiquitin into tau filaments in CBD and AD mediates inter-protofilament packing resulting in distinct ultrastructural polymorphs, tuning the ratio of fibril subtypes in tau inclusions.

filament structure by promoting its morphological transition toward straight filaments (Wang et al., 1996). It has also been reported that small, negatively charged molecules, such as ATP, can trigger the aggregation of 4R tau and, in a concentration-dependent manner, modulate the formation of singlet and doublet fibrils (Farid et al., 2014). This raises the possibility that additional co-factors may help shape the protein fold of distinct strains in multiple tauopathies.

In this work, and consistent with other studies (Falcon et al., 2018a, 2019; Fitzpatrick et al., 2017; Zhang et al., 2019b), it has been found that each tauopathy is associated with a disease-specific tau protofilament, which packs together predominantly in one of two ways to form a fibril. Many of these ultrastructural polymorphs exhibit packing between protofilaments that, in the absence of a small ligand or PTM, is extremely weak, with few tau protein backbone or direct sidechain contacts between protofilaments to stabilize the fibrillar structure (Iadanza et al., 2018a, 2018b).

The straight filament in AD has no salt bridges, hydrogen bonds, or hydrophobic packing holding the two protofilaments together (Figure S6B), and tau molecules in mating protofilaments form small interfaces with each other (82 $Å^2$ per inter-protofilament β strand contact). By cryo-EM (Figures 6C, S6B, and S6C) and MS (Figure 3), we find that the C terminus of ubiquitin stabilizes the inter-protofilament interface in straight tau filaments from AD, suggesting that mono- and poly-ubiquitin chains form a stable and critical component of the fibril core (Figure 6D).

The two protofilaments in doublet fibrils formed by tau in CBD are only connected via two bifurcated hydrogen bonds (Figure 2B), which are ~50% weaker than canonical hydrogen bonds (Feldblum and Arkin, 2014) with few interfacial tau-tau contacts (63 $Å^2$ per inter-protofilament β strand contact). Given that there are intense, non-tau densities near K_{353} at the inter-protofilament interface of doublet fibrils in CBD (Figures 2B, 2C, and 6A), similar in size to those found at K_{311} and $K_{317/321}$ in straight filaments in AD (Figure 6C), we speculate that mono- and poly-ubiquitin chains may also play a structural role in stabilizing this ultrastructural polymorph (Figure 6B).

We propose a structure-based model in which the incorporation of ubiquitin into tau filaments in CBD and AD mediates specific inter-protofilament packing, resulting in distinct ultrastructural polymorphs (Figure 7). Ubiquitination may help stabilize inter-protofilament packing by providing additional contacts between tau molecules in each protofilament via ubiquitin chains, thereby favoring the formation of these fibril subtypes (Figure 7). Not only do mono- and poly-ubiquitination between the protofilaments add considerably more interfacial contacts, but they also increase the likelihood of sidechain-backbone and sidechain-sidechain hydrogen bonding between tau protofilaments and ubiquitin molecules. This may also be the case for other tau filaments such as the wide PiD filament (Falcon et al., 2018a), which also has a remarkably weak inter-protofilament packing (only 38 $Å^2$ per inter-protofilament β strand contact) (Iadanza et al., 2018b) and may be additionally stabilized by ubiquitinated K_{311}, K_{317}, K_{321}, and K_{331} sites in the immediate vicinity of the interface between protofilaments.

By contrast, if sites on tau critical to the formation of straight filaments in AD (K_{311} and $K_{317/321}$) or doublet fibrils in CBD (K_{353}) are acetylated, or ubiquitinated with low occupancy, the singlet fibril in CBD (Figures 5A and 5B) and paired helical filaments in AD (Figure S6A) adopt structures that do not require mediation by non-tau components at the inter-protofilament interface. The singlet fibril in CBD exists as a single protofilament (Figures 2, 5A, and 5B), and the paired helical filament has a strong, hexagonal hydrogen bonding network between its two protofilaments (Fitzpatrick et al., 2017). AD cases typically have a preponderance of paired helical filaments over straight filaments, but this ratio varies between patients and brain regions (Crowther, 1991; Falcon et al., 2018b). In CBD, we observe a ratio of singlet to doublet fibrils of approximately 1:2, but the inverse has also been reported (Ksiezak-Reding et al., 1996). We propose that the variation in fibril subtype populations may be mediated by cross-talk between PTMs, with ubiquitination at the inter-protofilament interface being a key modulator of ultrastructural polymorphism (Figure 7). The outcome of this structure-based model would be that neuronal inclusions and astrocytic plaques in CBD (Dickson et al., 2011) and neurofibrillary tangles and neuritic plaques in AD (Bloom, 2014) have a mixture of fibril subtypes whose populations are modulated by PTMs (Figure 7).

As the most abundant amino acid in the fibril cores of CBD and AD is lysine (15.9% and 14.3%, respectively), which makes acetylation or ubiquitination of tau highly likely (Kontaxi et al., 2017; Park et al., 2018; Petrucelli et al., 2004), it should be possible to systematically test *in vitro* whether PTMs are molecular determinants that favor specific ultrastructural polymorphs during nucleation and growth of tau filaments. In this vein, recent studies show distinct differences in aggregation kinetics, preferential proteasomal degradation, and filament structure between ubiquitinated and non-ubiquitinated repeats R1–R4 of tau and α-synuclein (Haj-Yahya et al., 2013; Ye et al., 2019). However, considering that heparin-induced recombinant tau filaments have been shown to form different structures than brain-derived tau filaments (Zhang et al., 2019a), such studies would require extensive optimization and validation to assess and ensure filament morphology accurately recapitulated brain-derived tau filaments. As such, our hybrid method of combining cryo-EM and MS of tau filaments from postmortem tissue is the most direct approach to elucidate the critical relationship between PTMs and fibril structure. This linkage is crucial to understanding fibril nucleation (Haj-Yahya et al., 2013; Ye et al., 2019), templating selectivity (Guo et al., 2016), tendencies to interact with other species intra- and extracellularly (Knowles et al., 2014), preferred sites of accumulation (Zempel et al., 2017), and differences in cell-specific vulnerability (Kaufman et al., 2016).

In conclusion, we have identified the importance of PTMs in mediating the distinct structures of tau fibrils in CBD and AD. This is consistent with the likelihood that PTMs are central to tauopathies and, given the long-lived nature of other proteins found aggregated in brains (Truscott et al., 2016), other strain-specific neurodegenerative diseases. We propose that our approach of combining cryo-EM with MS-based proteomics forms a methodological blueprint to fully decipher the role of PTMs in neurodegeneration.

STAR★METHODS

Detailed methods are provided in the online version of this paper and include the following:

- KEY RESOURCES TABLE
- LEAD CONTACT AND MATERIALS AVAILABILITY
  - Acquisition of Human Tissues
- EXPERIMENTAL MODEL AND SUBJECT DETAILS
  - Clinical history and pathology of CBD case 1
  - Clinical history and pathology of CBD case 2
  - Clinical history and pathology of AD case
- METHOD DETAILS
  - Immunohistochemistry
  - Preparation of Sarkosyl-insoluble Tau
  - Pronase treatment
  - Immuno-electron microscopy
  - Cryo-EM
  - Helical Reconstruction
  - Model Building and Refinement
  - Mass Spectrometry Analysis
  - Prediction of aggregation propensity
- QUANTIFICATION AND STATISTICAL ANALYSIS
- DATA AND CODE AVAILABILITY

SUPPLEMENTAL INFORMATION

Supplemental Information can be found online at https://doi.org/10.1016/j.cell.2020.01.027.

ACKNOWLEDGMENTS

We are exceedingly grateful to the patients and their families for their participation in this work. Human biological samples and associated data were obtained from the Mayo Clinic Brain Bank. This work was supported by the National Institutes of Health (NIH)/National Institute of Neurological Disorder and Stroke and the National Institute on Aging (UO1NS110438 and RF1AG056151-01A1 to A.W.P.F.; R35NS097273, U01NS110438-02, P01NS084974, P01NS099114, R01NS088689, RF1AG062077-01, RF1 AG062171-01, and U54NS100693 to L.P.; R01AG053960, R01AG061800, U01AG046161, and U01AG061357 to N.T.S.); the NSF MRI grant (1531991) for the ThermoFisher Titan Krios at the Eyring Materials center at ASU. We thank Prof. H. Zhou for use of the Titan Krios at UCLA EICN. This work was also supported by grants from the NIH (S10RR23057, S10OD018111, and U24GM116792) and the NSF (DBI-1338135 and DMR-1548924). We thank Dr. W.J. Rice for help collecting data on the Titan Krios at the NYU Langone Cryo-EM Core Facility; Dr. X. Chen and Dr. K. Song for help collecting data on the Titan Krios at the University of Massachusetts Medical School Cryo-EM Core Facility; R. Grassucci and Dr. Z. Zhang for help collecting data on the Columbia University Medical School Titan Krios housed at the Simons Electron Microscopy Center and National Resource for Automated Molecular Microscopy (New York Structural Biology Center) supported by grants from the Simons Foundation (349247), NYSTAR, and the NIH (GM103310); the Mayo Clinic Foundation; the Association for Frontotemporal Degeneration; the Dana Foundation; and the Cure Alzheimer's Fund. We thank Professor R.S. Mann for helpful discussions. This paper is dedicated to the memory of Professor Sir Christopher M. Dobson, F.R.S., Ph.D. advisor and mentor to A.W.P.F.

AUTHOR CONTRIBUTIONS

A.W.P.F., N.T.S., and L.P. conceived the experiments. D.W.D. and M.D. identified patients and performed neuropathology. Y.C. purified tau filaments from CBD and AD cases. A.W.P.F., T.A., and D.W. performed cryo-EM experiments on CBD and AD samples. D.M.D., S.R.K., and N.T.S. performed and analyzed mass spectrometry experiments. A.W.P.F., T.A., and K.W. processed cryo-EM data. A.W.P.F. and C.E.L. built atomic models. A.W.P.F, T.A., C.E.L., C.N.C., and L.P. prepared the manuscript. L.P. and A.W.P.F. supervised the project.

DECLARATION OF INTERESTS

The authors declare no competing interests.

Received: November 22, 2019
Revised: December 23, 2019
Accepted: January 21, 2020
Published: February 6, 2020

REFERENCES

Abreha, M.H., Dammer, E.B., Ping, L., Zhang, T., Duong, D.M., Gearing, M., Lah, J.J., Levey, A.I., and Seyfried, N.T. (2018). Quantitative Analysis of the Brain Ubiquitylome in Alzheimer's Disease. Proteomics *18*, e1800108.

Afonine, P.V., Poon, B.K., Read, R.J., Sobolev, O.V., Terwilliger, T.C., Urzhumtsev, A., and Adams, P.D. (2018). Real-space refinement in PHENIX for cryo-EM and crystallography. Acta Crystallogr. D Struct. Biol. *74*, 531–544.

Bai, B., Hales, C.M., Chen, P.C., Gozal, Y., Dammer, E.B., Fritz, J.J., Wang, X., Xia, Q., Duong, D.M., Street, C., et al. (2013). U1 small nuclear ribonucleoprotein complex and RNA splicing alterations in Alzheimer's disease. Proc. Natl. Acad. Sci. USA *110*, 16562–16567.

Ballatore, C., Lee, V.M., and Trojanowski, J.Q. (2007). Tau-mediated neurodegeneration in Alzheimer's disease and related disorders. Nat. Rev. Neurosci. *8*, 663–672.

Bloom, G.S. (2014). Amyloid-β and tau: the trigger and bullet in Alzheimer disease pathogenesis. JAMA Neurol. *71*, 505–508.

Boyer, D., and Eisenberg, D.S. (2019). A structure-based model for the electrostatic interaction of the N-terminus of protein tau with the fibril core of Alzheimer's disease filaments. Alzheimers Dement. *15*, 321.

Braak, H., and Braak, E. (1998). Argyrophilic grain disease: frequency of occurrence in different age categories and neuropathological diagnostic criteria. J. Neural Transm. (Vienna) *105*, 801–819.

Chen, V.B., Arendall, W.B., 3rd, Headd, J.J., Keedy, D.A., Immormino, R.M., Kapral, G.J., Murray, L.W., Richardson, J.S., and Richardson, D.C. (2010). MolProbity: all-atom structure validation for macromolecular crystallography. Acta Crystallogr. D Biol. Crystallogr. *66*, 12–21.

Chen, S., McMullan, G., Faruqi, A.R., Murshudov, G.N., Short, J.M., Scheres, S.H., and Henderson, R. (2013). High-resolution noise substitution to measure overfitting and validate resolution in 3D structure determination by single particle electron cryomicroscopy. Ultramicroscopy *135*, 24–35.

Cohen, T.J., Guo, J.L., Hurtado, D.E., Kwong, L.K., Mills, I.P., Trojanowski, J.Q., and Lee, V.M. (2011). The acetylation of tau inhibits its function and promotes pathological tau aggregation. Nat. Commun. *2*, 252.

Cripps, D., Thomas, S.N., Jeng, Y., Yang, F., Davies, P., and Yang, A.J. (2006). Alzheimer disease-specific conformation of hyperphosphorylated paired helical filament-Tau is polyubiquitinated through Lys-48, Lys-11, and Lys-6 ubiquitin conjugation. J. Biol. Chem. *281*, 10825–10838.

Crowther, R.A. (1991). Straight and paired helical filaments in Alzheimer disease have a common structural unit. Proc. Natl. Acad. Sci. USA *88*, 2288–2292.

Dickey, C.A., Yue, M., Lin, W.L., Dickson, D.W., Dunmore, J.H., Lee, W.C., Zehr, C., West, G., Cao, S., Clark, A.M., et al. (2006). Deletion of the ubiquitin ligase CHIP leads to the accumulation, but not the aggregation, of both endogenous phospho- and caspase-3-cleaved tau species. J. Neurosci. *26*, 6985–6996.

Dickson, D.W., Yen, S.H., Suzuki, K.I., Davies, P., Garcia, J.H., and Hirano, A. (1986). Ballooned neurons in select neurodegenerative diseases contain phosphorylated neurofilament epitopes. Acta Neuropathol. *71*, 216–223.

Dickson, D.W., Kouri, N., Murray, M.E., and Josephs, K.A. (2011). Neuropathology of frontotemporal lobar degeneration-tau (FTLD-tau). J. Mol. Neurosci. *45*, 384–389.

Dil Kuazi, A., Kito, K., Abe, Y., Shin, R.-W., Kamitani, T., and Ueda, N. (2003). NEDD8 protein is involved in ubiquitinated inclusion bodies. J. Pathol. *199*, 259–266.

Eisenberg, D., and Jucker, M. (2012). The amyloid state of proteins in human diseases. Cell *148*, 1188–1203.

Emsley, P., Lohkamp, B., Scott, W.G., and Cowtan, K. (2010). Features and development of Coot. Acta Crystallogr. D Biol. Crystallogr. *66*, 486–501.

Ercan, E., Eid, S., Weber, C., Kowalski, A., Bichmann, M., Behrendt, A., Matthes, F., Krauss, S., Reinhardt, P., Fulle, S., and Ehrnhoefer, D.E. (2017). A validated antibody panel for the characterization of tau post-translational modifications. Mol. Neurodegener. *12*, 87.

Falcon, B., Zhang, W., Murzin, A.G., Murshudov, G., Garringer, H.J., Vidal, R., Crowther, R.A., Ghetti, B., Scheres, S.H.W., and Goedert, M. (2018a). Structures of filaments from Pick's disease reveal a novel tau protein fold. Nature *561*, 137–140.

Falcon, B., Zhang, W., Schweighauser, M., Murzin, A.G., Vidal, R., Garringer, H.J., Ghetti, B., Scheres, S.H.W., and Goedert, M. (2018b). Tau filaments from multiple cases of sporadic and inherited Alzheimer's disease adopt a common fold. Acta Neuropathol. *136*, 699–708.

Falcon, B., Zivanov, J., Zhang, W., Murzin, A.G., Garringer, H.J., Vidal, R., Crowther, R.A., Newell, K.L., Ghetti, B., Goedert, M., and Scheres, S.H.W. (2019). Novel tau filament fold in chronic traumatic encephalopathy encloses hydrophobic molecules. Nature *568*, 420–423.

Farid, M., Corbo, C.P., and Alonso, Adel.C. (2014). Tau binds ATP and induces its aggregation. Microsc. Res. Tech. *77*, 133–137.

Feany, M.B., and Dickson, D.W. (1995). Widespread cytoskeletal pathology characterizes corticobasal degeneration. Am. J. Pathol. *146*, 1388–1396.

Feldblum, E.S., and Arkin, I.T. (2014). Strength of a bifurcated H bond. Proc. Natl. Acad. Sci. USA *111*, 4085–4090.

Fitzpatrick, A.W.P., and Saibil, H.R. (2019). Cryo-EM of amyloid fibrils and cellular aggregates. Curr. Opin. Struct. Biol. *58*, 34–42.

Fitzpatrick, A.W.P., Debelouchina, G.T., Bayro, M.J., Clare, D.K., Caporini, M.A., Bajaj, V.S., Jaroniec, C.P., Wang, L., Ladizhansky, V., Müller, S.A., et al. (2013). Atomic structure and hierarchical assembly of a cross-β amyloid fibril. Proc. Natl. Acad. Sci. USA *110*, 5468–5473.

Fitzpatrick, A.W.P., Falcon, B., He, S., Murzin, A.G., Murshudov, G., Garringer, H.J., Crowther, R.A., Ghetti, B., Goedert, M., and Scheres, S.H.W. (2017). Cryo-EM structures of tau filaments from Alzheimer's disease. Nature *547*, 185–190.

Goedert, M., Falcon, B., Zhang, W., Ghetti, B., and Scheres, S.H.W. (2018). Distinct Conformers of Assembled Tau in Alzheimer's and Pick's Diseases. Cold Spring Harb. Symp. Quant. Biol. *83*, 163–171.

Guo, J.L., Narasimhan, S., Changolkar, L., He, Z., Stieber, A., Zhang, B., Gathagan, R.J., Iba, M., McBride, J.D., Trojanowski, J.Q., and Lee, V.M. (2016). Unique pathological tau conformers from Alzheimer's brains transmit tau pathology in nontransgenic mice. J. Exp. Med. *213*, 2635–2654.

Haj-Yahya, M., Fauvet, B., Herman-Bachinsky, Y., Hejjaoui, M., Bavikar, S.N., Karthikeyan, S.V., Ciechanover, A., Lashuel, H.A., and Brik, A. (2013). Synthetic polyubiquitinated α-Synuclein reveals important insights into the roles of the ubiquitin chain in regulating its pathophysiology. Proc. Natl. Acad. Sci. USA *110*, 17726–17731.

He, S., and Scheres, S.H.W. (2017). Helical reconstruction in RELION. J. Struct. Biol. *198*, 163–176.

Higginbotham, L., Ping, L., Dammer, E.B., Duong, D.M., Zhou, M., Gearing, M., Johnson, E.C.B., Hajjar, I., Lah, J.J., Levey, A.I., et al. (2019). Integrated Proteomics Reveals Brain-Based Cerebrospinal Fluid Biomarkers in Asymptomatic and Symptomatic Alzheimer's Disease. bioRxiv. https://doi.org/10.1101/806752.

Iadanza, M.G., Jackson, M.P., Hewitt, E.W., Ranson, N.A., and Radford, S.E. (2018a). A new era for understanding amyloid structures and disease. Nat. Rev. Mol. Cell Biol. *19*, 755–773.

Iadanza, M.G., Silvers, R., Boardman, J., Smith, H.I., Karamanos, T.K., Debelouchina, G.T., Su, Y., Griffin, R.G., Ranson, N.A., and Radford, S.E. (2018b). The structure of a β_2-microglobulin fibril suggests a molecular basis for its amyloid polymorphism. Nat. Commun. *9*, 4517.

Irwin, D.J. (2016). Tauopathies as clinicopathological entities. Parkinsonism Relat. Disord. *22* (*Suppl 1*), S29–S33.

Irwin, D.J., Cohen, T.J., Grossman, M., Arnold, S.E., Xie, S.X., Lee, V.M., and Trojanowski, J.Q. (2012). Acetylated tau, a novel pathological signature in Alzheimer's disease and other tauopathies. Brain *135*, 807–818.

Kam, T.-I., Mao, X., Park, H., Chou, S.-C., Karuppagounder, S.S., Umanah, G.E., Yun, S.P., Brahmachari, S., Panicker, N., Chen, R., et al. (2018). Poly(ADP-ribose) drives pathologic α-synuclein neurodegeneration in Parkinson's disease. Science *362*, eaat8407.

Kamieniarz, K., and Schneider, R. (2009). Tools to tackle protein acetylation. Chem. Biol. *16*, 1027–1029.

Kaufman, S.K., Sanders, D.W., Thomas, T.L., Ruchinskas, A.J., Vaquer-Alicea, J., Sharma, A.M., Miller, T.M., and Diamond, M.I. (2016). Tau Prion Strains Dictate Patterns of Cell Pathology, Progression Rate, and Regional Vulnerability In Vivo. Neuron *92*, 796–812.

Kidd, M. (1963). Paired helical filaments in electron microscopy of Alzheimer's disease. Nature *197*, 192–193.

Knowles, T.P., Vendruscolo, M., and Dobson, C.M. (2014). The amyloid state and its association with protein misfolding diseases. Nat. Rev. Mol. Cell Biol. *15*, 384–396.

Kollmer, M., Close, W., Funk, L., Rasmussen, J., Bsoul, A., Schierhorn, A., Schmidt, M., Sigurdson, C.J., Jucker, M., and Fändrich, M. (2019). Cryo-EM structure and polymorphism of Aβ amyloid fibrils purified from Alzheimer's brain tissue. Nat. Commun. *10*, 4760.

Kontaxi, C., Piccardo, P., and Gill, A.C. (2017). Lysine-Directed Post-translational Modifications of Tau Protein in Alzheimer's Disease and Related Tauopathies. Front. Mol. Biosci. *4*, 56.

Krissinel, E., and Henrick, K. (2007). Inference of macromolecular assemblies from crystalline state. J. Mol. Biol. *372*, 774–797.

Ksiezak-Reding, H., Tracz, E., Yang, L.S., Dickson, D.W., Simon, M., and Wall, J.S. (1996). Ultrastructural instability of paired helical filaments from corticobasal degeneration as examined by scanning transmission electron microscopy. Am. J. Pathol. *149*, 639–651.

Kucukelbir, A., Sigworth, F.J., and Tagare, H.D. (2014). Quantifying the local resolution of cryo-EM density maps. Nat. Methods *11*, 63–65.

Lee, M.J., Lee, J.H., and Rubinsztein, D.C. (2013). Tau degradation: the ubiquitin-proteasome system versus the autophagy-lysosome system. Prog. Neurobiol. *105*, 49–59.

Losev, Y., Paul, A., Frenkel-Pinter, M., Abu-Hussein, M., Khalaila, I., Gazit, E., and Segal, D. (2019). Novel model of secreted human tau protein reveals the impact of the abnormal N-glycosylation of tau on its aggregation propensity. Sci. Rep. *9*, 2254.

Luo, H.B., Xia, Y.Y., Shu, X.J., Liu, Z.C., Feng, Y., Liu, X.H., Yu, G., Yin, G., Xiong, Y.S., Zeng, K., et al. (2014). SUMOylation at K340 inhibits tau degradation through deregulating its phosphorylation and ubiquitination. Proc. Natl. Acad. Sci. USA *111*, 16586–16591.

Mandelkow, E.M., and Mandelkow, E. (2012). Biochemistry and cell biology of tau protein in neurofibrillary degeneration. Cold Spring Harb. Perspect. Med. *2*, a006247.

Min, S.W., Cho, S.H., Zhou, Y., Schroeder, S., Haroutunian, V., Seeley, W.W., Huang, E.J., Shen, Y., Masliah, E., Mukherjee, C., et al. (2010). Acetylation of tau inhibits its degradation and contributes to tauopathy. Neuron *67*, 953–966.

Morris, M., Knudsen, G.M., Maeda, S., Trinidad, J.C., Ioanoviciu, A., Burlingame, A.L., and Mucke, L. (2015). Tau post-translational modifications in wild-type and human amyloid precursor protein transgenic mice. Nat. Neurosci. *18*, 1183–1189.

Myeku, N., Clelland, C.L., Emrani, S., Kukushkin, N.V., Yu, W.H., Goldberg, A.L., and Duff, K.E. (2016). Tau-driven 26S proteasome impairment and cognitive dysfunction can be prevented early in disease by activating cAMP-PKA signaling. Nat. Med. *22*, 46–53.

Park, S., Lee, J.H., Jeon, J.H., and Lee, M.J. (2018). Degradation or aggregation: the ramifications of post-translational modifications on tau. BMB Rep. *51*, 265–273.

Perez-Riverol, Y., Csordas, A., Bai, J., Bernal-Llinares, M., Hewapathirana, S., Kundu, D.J., Inuganti, A., Griss, J., Mayer, G., Eisenacher, M., et al. (2019). The PRIDE database and related tools and resources in 2019: improving support for quantification data. Nucleic Acids Res. *47* (D1), D442–D450.

Petkova, A.T., Leapman, R.D., Guo, Z., Yau, W.M., Mattson, M.P., and Tycko, R. (2005). Self-propagating, molecular-level polymorphism in Alzheimer's beta-amyloid fibrils. Science *307*, 262–265.

Petrucelli, L., Dickson, D., Kehoe, K., Taylor, J., Snyder, H., Grover, A., De Lucia, M., McGowan, E., Lewis, J., Prihar, G., et al. (2004). CHIP and Hsp70 regulate tau ubiquitination, degradation and aggregation. Hum. Mol. Genet. *13*, 703–714.

Pettersen, E.F., Goddard, T.D., Huang, C.C., Couch, G.S., Greenblatt, D.M., Meng, E.C., and Ferrin, T.E. (2004). UCSF Chimera–a visualization system for exploratory research and analysis. J. Comput. Chem. *25*, 1605–1612.

Schrödinger, L.L.C. (2017). The PyMOL Molecular Graphics System, Version 2.0.

Sergeant, N., Wattez, A., and Delacourte, A. (1999). Neurofibrillary degeneration in progressive supranuclear palsy and corticobasal degeneration: tau pathologies with exclusively "exon 10" isoforms. J. Neurochem. *72*, 1243–1249.

Sormanni, P., Aprile, F.A., and Vendruscolo, M. (2015). The CamSol method of rational design of protein mutants with enhanced solubility. J. Mol. Biol. *427*, 478–490.

Swaney, D.L., McAlister, G.C., and Coon, J.J. (2008). Decision tree-driven tandem mass spectrometry for shotgun proteomics. Nat. Methods *5*, 959–964.

Terry, R.D. (1963). The Fine Structure of Neurofibrillary Tangles in Alzheimer's Disease. J. Neuropathol. Exp. Neurol. *22*, 629–642.

Tracz, E., Dickson, D.W., Hainfeld, J.F., and Ksiezak-Reding, H. (1997). Paired helical filaments in corticobasal degeneration: the fine fibrillary structure with NanoVan. Brain Res. *773*, 33–44.

Truscott, R.J.W., Schey, K.L., and Friedrich, M.G. (2016). Old Proteins in Man: A Field in its Infancy. Trends Biochem. Sci. *41*, 654–664.

Trzeciakiewicz, H., Tseng, J.H., Wander, C.M., Madden, V., Tripathy, A., Yuan, C.X., and Cohen, T.J. (2017). A Dual Pathogenic Mechanism Links Tau Acetylation to Sporadic Tauopathy. Sci. Rep. *7*, 44102.

Wang, J.Z., Grundke-Iqbal, I., and Iqbal, K. (1996). Glycosylation of microtubule-associated protein tau: an abnormal posttranslational modification in Alzheimer's disease. Nat. Med. *2*, 871–875.

Warnecke, A., Sandalova, T., Achour, A., and Harris, R.A. (2014). PyTMs: a useful PyMOL plugin for modeling common post-translational modifications. BMC Bioinformatics *15*, 370.

Ye, Y., Klenerman, D., and Finley, D. (2019). N-Terminal Ubiquitination of Amyloidogenic Proteins Triggers Removal of Their Oligomers by the Proteasome Holoenzyme. J. Mol. Biol. https://doi.org/10.1016/j.jmb.2019.08.021.

Zempel, H., Dennissen, F.J.A., Kumar, Y., Luedtke, J., Biernat, J., Mandelkow, E.M., and Mandelkow, E. (2017). Axodendritic sorting and pathological missorting of Tau are isoform-specific and determined by axon initial segment architecture. J. Biol. Chem. *292*, 12192–12207.

Zhang, K. (2016). Gctf: Real-time CTF determination and correction. J. Struct. Biol. *193*, 1–12.

Zhang, W., Falcon, B., Murzin, A.G., Fan, J., Crowther, R.A., Goedert, M., and Scheres, S.H. (2019a). Heparin-induced tau filaments are polymorphic and differ from those in Alzheimer's and Pick's diseases. eLife *8*, e43584.

Zhang, W., Tarutani, A., Newell, K.L., Murzin, A.G., Matsubara, T., Falcon, B., Vidal, R., Garringer, H.J., Shi, Y., Ikeuchi, T., et al. (2019b). Novel tau filament fold in corticobasal degeneration, a four-repeat tauopathy. bioRxiv. https://doi.org/10.1101/811703.

Zheng, S.Q., Palovcak, E., Armache, J.P., Verba, K.A., Cheng, Y., and Agard, D.A. (2017). MotionCor2: anisotropic correction of beam-induced motion for improved cryo-electron microscopy. Nat. Methods *14*, 331–332.

STAR★METHODS

KEY RESOURCES TABLE

REAGENT or RESOURCE	SOURCE	IDENTIFIER
Antibodies		
Mouse monoclonal anti-pTau (phosphorylated at Ser202)	P. Davies, Albert Einstein College of Medicine; New York, NY; USA	CP13; RRID: AB_2314223
Mouse monoclonal anti-pTau (phosphorylated at Ser396 and Ser404)	P. Davies, Albert Einstein College of Medicine; New York, NY; USA	PHF1; RRID: AB_2315150
Mouse monoclonal anti-pTau (phosphorylated at Ser262 and Ser356)	P. Seubert, Elan Pharmaceuticals; San Francisco, CA; USA	12E8
Rabbit polyclonal anti-Tau (Human-specific)	L. Petrucelli, Mayo Clinic; Jacksonville, FL; USA	E1; RRID: 2819185
Mouse monoclonal anti-Tau (Tau46)	Sigma	Cat#T9450; RRID: AB_477595
Mouse monoclonal anti-ubiquitin (Ubi-1)	Millipore	Cat#MAB1510; RRID: AB_2180556
6nm colloidal gold-conjugated goat anti-mouse	Jackson ImmunoResearch	Cat#115-195-146; RRID: AB_2338728
6nm colloidal gold-conjugated goat anti-rabbit	Jackson ImmunoResearch	Cat#111-195-144; RRID: AB_2338015
peroxidase-conjugated donkey anti-rabbit	Jackson ImmunoResearch	Cat#711-036-152; RRID: AB_2340590
peroxidase-conjugated donkey anti-mouse	Jackson ImmunoResearch	Cat#715-036-150; RRID: AB_2340773
formvar/carbon copper grids 400 mesh	Electron Microscopy Sciences	FCF400-Cu
Biological Samples		
AD frontal cortex tissue	Mayo Clinic Brain Bank	https://www.mayo.edu/research/departments-divisions/department-neuroscience-florida/brain-bank
CBD frontal cortex tissue	Mayo Clinic Brain Bank	https://www.mayo.edu/research/departments-divisions/department-neuroscience-florida/brain-bank
Chemicals, Peptides, and Recombinant Proteins		
Protease inhibitor cocktail	Millipore	Cat#539131
Phosphatase inhibitor cocktail	Bimake	Cat#B15002
Pronase	Millipore	Cat#537088
Deposited Data		
Raw mass spectrometry data	This paper	ProteomeXchange PXD016862
Raw mass spectrometry data	This paper	Synapse Sage Bionetworks www.synapse.org/#!Synapse:syn2397898
Cryo-EM density map of CBD singlet	This paper	EMD-21201
Cryo-EM density map of CBD doublet	This paper	EMD-21200
Cryo-EM density map of AD paired helical filament	This paper	EMD-21207
Atomic model of CBD singlet	This paper	PDB: 6VHA
Atomic model of CBD doublet	This paper	PDB: 6VH7
Atomic model of AD paired helical filament	This paper	PDB: 6VHL
Atomic model of AD straight filament	This paper	PDB: 6VI3
Software and Algorithms		
MotionCor2	(Zheng et al., 2017)	https://msg.ucsf.edu/software
Gctf v1.06	(Zhang, 2016)	https://www.mrc-lmb.cam.ac.uk/kzhang/Gctf/
RELION	(He and Scheres, 2017)	https://www2.mrc-lmb.cam.ac.uk/relion
Chimera	(Pettersen et al., 2004)	https://www.cgl.ucsf.edu/chimera/

(*Continued on next page*)

Continued

REAGENT or RESOURCE	SOURCE	IDENTIFIER
Coot	(Emsley et al., 2010)	https://www2.mrc-lmb.cam.ac.uk/personal/pemsley/coot/
Phenix.real_space_refine (v1.17.1-3660)	(Afonine et al., 2018)	https://www.phenix-online.org/
MolProbity	(Chen et al., 2010)	http://molprobity.biochem.duke.edu/
Phenix: Isopeptide bond-length restraints (v1.17.1-3660)	(Afonine et al., 2018)	https://www.phenix-online.org/
Proteome Discoverer 2.3 (Percolator)	ThermoFisher	
CamSol method	(Sormanni et al., 2015)	http://www-vendruscolo.ch.cam.ac.uk/camsolmethod.html
PyTMs	(Warnecke et al., 2014)	https://pymolwiki.org/index.php/Pytms
PyMOL	(Schrödinger, 2017)	https://.pymol.org
PISA server	(Krissinel and Henrick, 2007)	https://www.ebi.ac.uk/pdbe/pisa/
Other		
Holey carbon grids (Au R1.2/1.3, 300 mesh)	Quantifoil	N/A
BioRender	N/A	https://biorender.com/

LEAD CONTACT AND MATERIALS AVAILABILITY

Further information and requests for resources and reagents should be directed to and will be fulfilled by the Lead Contact, Anthony W.P. Fitzpatrick (Anthony.Fitzpatrick@columbia.edu). All unique/stable reagents generated in this study are available from the Lead Contact without restriction.

Acquisition of Human Tissues

Human brain samples were collected under a Mayo Clinic IRB-approved autopsy protocol. Tissues were de-identified prior to use, with no identifiers to patient names linked to brain samples. Patient confidentiality is strictly kept. As such, the utilization of autopsy-derived, de-identified human brain tissue in the current study is exempt from IRB regulations. All tissue was handled with universal precautions. For human postmortem brain tissue requests from the Mayo Clinic Brain Bank, see https://www.mayo.edu/research/departments-divisions/department-neuroscience-florida/brain-bank.

EXPERIMENTAL MODEL AND SUBJECT DETAILS

Clinical history and pathology of CBD case 1

The patient was a 61-year-old woman with no family history of neurological disease. She had a five-year history of progressive aphasia as well as behavioral variant frontotemporal dementia characterized by impulse control disorder, antisocial behavior, hoarding disorder, and an inability to perform household tasks. Upon neurological examination, the patient exhibited flat effect, speech latency, and simplistic speech output. She was unable to perform simple calculations such as serial 7's and demonstrated markedly slow motor responses. Her memory remained relatively intact. Formal neuropsychological testing showed deficits in processing speed and set-shifting. She was severely impaired on a card sorting test as well as tests of semantic and letter fluency. Magnetic resonance imaging scans exhibited mild ventricular enlargement and mild cortical atrophy. Fluorodeoxyglucose positron emission tomography spectroscopy showed bilateral decreased uptake in medial and inferior frontal cortices and anterior cingulate gyri as well as asymmetrical uptake in left middle frontal and sensorimotor cortices. Upon progression of the disease, patient developed severe aphasia and became limited to simple one-word responses.

During autopsy, the brain was cleaved in half. The left half was frozen, whereas the right hemibrain was dissected. The calculated whole brain weight equaled 1080 g. The sulci and gyri revealed circumscribed cortical atrophy most marked in superior frontal gyrus, middle frontal gyrus, and opercular portion of inferior frontal gyrus. Medial temporal lobe structures were unremarkable. Coronal sections of the brain showed marked enlargement of frontal and temporal horns of the lateral ventricle. There was mild atrophy of the caudate nucleus and the dorsomedial thalamus. The substantia nigra had mild decreased pigmentation. Histologic studies of the frontal lobe, especially the superior frontal gyrus, revealed cortical atrophy with spongiosis, gliosis, and ballooned neurons. Ballooned neurons were most numerous in superior frontal and cingulate gyri. Tau immunohistochemistry showed extensive neuronal and glial tau pathology as well as numerous neuropil threads in gray and white matter of cortical and subcortical structures. Cortical and subcortical neuronal inclusions were pleomorphic, with many astrocytic plaques in affected cortices of the frontal lobe and the striatum. The pathology was an archetypal example of CBD. No Alzheimer-type pathology was observed (Braak stage I, Thal phase 0).

Clinical history and pathology of CBD case 2

This 58-year-old white man developed progressive difficulty speaking and moving four years before he died. He became argumentative, and he showed poor judgement. This was followed by increasing apathy. He had a neurologic work-up, including MRI brain scan and an EEG, which were unrevealing. His progressive language problems were characterized by delays in responding and word finding difficulties. He developed obsessive behaviors, such as checking door locks and excessive hand washing. He showed decreased concern for personal hygiene. He had no significant past medical history, and his family history was negative for neurologic disease. On neurologic examination, he had latency to initiate speech and slow speech. He had no speech apraxia. He was fully oriented. He scored 29/30 on the Mini-Mental State Exam. His cranial nerve examination was normal except for mild masked facies, slow saccades in the vertical plane and hypophonia. His general motor examination was notable for increased tone in the extremities and slowing on finger tapping. There were no abnormal reflexes. He scored high on the Geriatric Depression Scale. Neuropsychologic testing was notable for mild dementia (Dementia Rating Scale-2 = 114/144) with decreases in word fluency, verbal memory, visual learning and executive dysfunction. He had progressive neurological decline with features of frontal executive dysfunction, behavioral and personality changes, as well as Parkinsonism with slurred speech. The major differential diagnosis was frontotemporal dementia versus progressive supranuclear palsy.

The fixed brain weight was 1140 g. The cerebral hemisphere had mild atrophy over the frontal convexity, most marked in the parasagittal and medial superior frontal gyrus. The medial temporal lobe was free of atrophy. Coronal sections revealed mild enlargement of the frontal horn of the lateral ventricle. The basal ganglia were unremarkable and the subthalamic nucleus had mild atrophy. There was marked pigment loss in the substantia nigra. Histologic sections showed cortical atrophy with spongiosis, gliosis, and ballooned neurons, most marked in superior frontal and cingulate gyri. There were no Alzheimer-type lesions with thioflavin S fluorescent microscopy, only isolated medial temporal neurofibrillary tangles (Braak NFT Stage 1, Thal amyloid phase 0). Tau immunohistochemistry showed neuronal and glial tauopathy consistent with cortical basal degeneration, including ballooned cortical neurons, many neuropil threads, pleomorphic small neuronal inclusions, and ballooned neurons in the limbic and frontal lobes.

Clinical history and pathology of AD case

This 68-year-old man had a 12-year history of progressive cognitive impairment with anxiety and behavioral disturbance, characterized by agitation and aggression. He was unable to remain gainfully employed. He previously worked as a cable splicer for a telephone company. He was involuntarily institutionalized several times due to behavioral problems. He was treated with Clonazepam, Namenda, Risperdal, trazadone, and Effexor. There was no family history of neurologic disorder. His review of systems was unremarkable. His general neurological exam was within normal limits, except for disorientation and severe memory deficits, especially affecting short term memory. There were no motor signs or symptoms. Neuroimaging studies (Figure S5) showed sulcal enlargement and dilated ventricles consistent with brain atrophy but no focal lesions. At autopsy, his brain weighed 1040 g (normal lower limit for men: 1200 g). There was severe Alzheimer-type pathology (Braak neurofibrillary tangle stage - VI, Thal amyloid phase - 5, CERAD neuritic plaque score - frequent). There were no Lewy bodies.

METHOD DETAILS

Immunohistochemistry

Paraffin-embedded tissue sections were deparaffinized in xylene and rehydrated through a series of ethanol solutions. Antigen retrieval was performed by steaming in distilled water for 30 min. Sections were then immunostained with CP13 or PHF1 (tau phospho-specific antibodies provided by Dr. Peter Davies, Albert Einstein College of Medicine) using the DAKO Autostainer (Universal Staining System) and the DAKO EnVision + HRP system. Sections were counterstained with hematoxylin, dehydrated through a series of ethanol and xylene washes, and coverslipped with Cytoseal mounting media (Thermo Fisher Scientific, Inc).

Preparation of Sarkosyl-insoluble Tau

Frozen CBD and AD tissue from the medial frontal cortex were homogenized separately in 10 volumes (w/v) of cold buffer consisting of 10 mM Tris-HCl (pH 7.4), 80 mM NaCl, 1 mM MgCl, 1 mM EGTA, 0.1 mM EDTA, 1 mM PMSF, 1 mM Dithiothreitol, and a protease and phosphatase inhibitor cocktail. The homogenized samples were split into aliquots and ultracentrifuged for 40 min at 4°C in a TLA110 rotor at 60,000 rpm. The pellets were resuspended in one volume of cold buffer (10 mM Tris (pH 7.4), 0.85 M NaCl, 10% (w/v) sucrose, 1 mM EGTA), and subsequently ultracentrifuged at 14,000 g for 10 min at 4°C. The supernatant was incubated with sarkosyl at a final concentration of 1% (w/v) for 1 h at room temperature with continuous agitation. Following this incubation, the samples were ultracentrifuged for 40 min at 4°C in a TLA110 rotor at 60,000 rpm. The pellets (P3 fraction) were saved as the sarkosyl-insoluble material, which was snap frozen on dry ice and stored at −80°C. Western blot using tau antibodies PHF1 (pS396/404), Tau46 (aa404-441), 12E8 (pS262, pS356), E1 (aa19-33), and CP13 (pS202) was utilized to evaluate sarkosyl-insoluble tau from the CBD samples.

Pronase treatment

Sarkosyl-insoluble material was resuspended in TBS, and following determination of tau concentrations, 50 ng tau from each sample was incubated in the presence or absence of pronase (Millipore) at 37°C. Protease inhibitor cocktail was then added to stop the reaction at either 1, 2, or 5 min. Pronase-treated and untreated samples were then spotted onto a nitrocellulose membrane to evaluate immunoreactivity for ubiquitin and tau antibodies. Briefly, dot blots were washed in TBS plus 0.1% (v/v) Triton-X (TBS-T) and incubated overnight at 4°C with the primary antibodies, Ubi-1, E1 (aa19-33), CP13 (pS202), 12E8, PHF1, and Tau46 (aa404-441). The following day, blots were washed in TBS-T, incubated with donkey anti-rabbit or anti-mouse IgG secondary antibodies conjugated to horseradish peroxidase (1:5000; Jackson ImmunoResearch) for 1 hour, and again washed with TBS-T. Protein expression was then visualized by enhanced chemiluminescence treatment and exposure to film.

Immuno-electron microscopy

Sarkosyl-insoluble material was resuspended in PBS and adsorbed onto carbon/formvar-coated 400 mesh copper grids (Electron Microscopy Sciences, Hatfield, PA) for 90 s. The grids were washed two times in TBS buffer, and blocked with 1 mg/mL BSA (w/v) in TBS buffer for 30 min at room temperature in a humidified chamber. Tau antibodies, E1 (aa19-33), Tau46 (aa404-441), and CP13 (pS202) as well as tau phospho-specific antibodies, PHF1 and 12E8, and a ubiquitin-specific antibody, Ubi-1, were used as primary antibodies. Primary antibody was applied (1:50 dilution in 1 mg/mL BSA (w/v) in TBS) for 1 hour and then washed three times in TBS buffer. Secondary gold-conjugated antibody was applied (1:20 dilution in 1 mg/mL BSA (w/v) in TBS) for 45 min and washed 6 times with TBS buffer. Grids were then stained with 2% (w/v) uranyl acetate (Electron Microscopy Sciences, Hatfield, PA) for 60 s and examined with a Philips 208S electron microscope (Philips, Hillsboro, OR).

Cryo-EM

Glow-discharged holey carbon grids (Quantifoil Au R1.2/1.3, 300 mesh) with 3 μL aliquots of purified tau filaments from CBD (< 0.1 mg/mL) or AD (1 mg/mL) were blotted with filter paper to remove excess sample. Using an FEI Vitrobot Mark IV, grids were plunge-frozen in liquid ethane and then imaged using an FEI Titan Krios at 300 kV with a Gatan K2 Summit detector in counting mode. Inelastically scattered electrons were removed with a GIF-quantum energy filter (Gatan) set at a slit width of 20 eV. Movie frames were recorded with an exposure time of 200 ms at a dose rate of 1.5 electrons per A^2 per frame for a total dose of 60 electrons per A^2 at a pixel size of 1.06 A. The resulting datasets comprised of 30,804 micrographs of tau fibrils in CBD and 20,382 micrographs of tau fibrils in AD, both with defocus values ranging from -1.0 to -3.0 μm.

Helical Reconstruction

Movie frames were gain-corrected, aligned, dose-weighted, and then summed into a single micrograph using MOTIONCOR2 (Zheng et al., 2017). The micrographs were used to estimate the contrast transfer function (CTF) using Gctf (Zhang, 2016). All subsequent image-processing steps were performed using helical reconstruction methods in RELION (He and Scheres, 2017) as previously described (Fitzpatrick et al., 2017) with minor changes as outlined below.

Fibrils were manually selected and separated into doublet and singlet populations based on maximum width. Since we collected data on CBD fibrils at four separate cryo-EM facilities, we down-scaled all fibrils to a pixel size of 1.414 Å to mitigate the effect of small variations in magnification on different microscopes. Initial models of the fibril subtypes were generated from pitch-views of the filaments, using an elongated ribbon as a starting reference. Using these initial models, 3D classification with $T = 50$ was used to refine a doublet fibril with a helical twist of $-0.6°$ and rise of 4.8 Å, consistent with an average crossover distance of approximately 1,300 Å. The doublet showed a clear 2-fold symmetry, and this was enforced, resulting in higher resolution. Refinement with C1 symmetry left the extra densities decorating the fibril unchanged from the C2-refinement. The singlet was refined with a helical twist of $-0.85°$ and rise of 4.8 Å, consistent with an average crossover distance of approximately 1,050 Å. Both maps were 3D autorefined and postprocessed in RELION (He and Scheres, 2017). AD fibrils were processed in a manner identical to (Fitzpatrick et al., 2017) with a helical twist of 179.42° and rise of 2.35 Å. Final overall resolution estimates of 3.8 Å (Doublet Fibril), 4.3 Å (Singlet Fibril), and 3.3 Å (Paired Helical Filament) were calculated from Fourier shell correlations at 0.143 between the two independently refined half-maps (Chen et al., 2013). Local resolution estimates were displayed using Resmap (Kucukelbir et al., 2014).

Model Building and Refinement

K_{274}-E_{380} was built by manually adding amino acids into the doublet fibril map, followed by real-space refinement in COOT (Emsley et al., 2010). First, a combination of the sharpened and masked singlet fibril and doublet fibril maps was used to trace a polyalanine chain into one rung of the protofilament density. Next, backbone geometries were refined using COOT, and sidechains K_{281}-V_{363} were added and real-space refined into the density. The extended conformation of $_{332}$PGGG$_{335}$ and $_{364}$PGGG$_{367}$ was initially modeled using the polyglycine II region from PDB-entry 5O3L. N- and C-terminal β strands were initially modeled using V_{275}-K_{280} from PDB-entry 5V5C (β1) and N_{368}-F_{378} from PDB-entry 5O3L (β11). A protein stack consisting of three identical rungs (chains E, F, and G) separated by 4.8 Å was assembled, and this protofilament was fitted into the doublet map using CHIMERA (Pettersen et al., 2004). A second copy of this protofilament (chains A, B, and C) was made and fitted into the C2-related protofilament density in the doublet map, making a total of 6 chains. For the doublet fibril structure, we used phenix.real_space_refine for model refinement (Afonine et al., 2018). Secondary structure, non-crystallographic symmetry, and hydrogen bond restraints were applied during refinement. The final doublet fibril model was validated using MolProbity (Chen et al., 2010). Since the resolution of the cryo-EM reconstruction of the singlet fibril is 4.3 Å, one protofilament of the doublet atomic model (chains E, F, and G) was rigid-body fitted into this map in CHIMERA. Paired helical filaments were built and refined in an identical manner to (Fitzpatrick et al., 2017) with the exception that covalent linkages to $_{76}$GG$_{75}$ have been incorporated into our atomic models at K_{317} using isopeptide bond-length restraints in Phenix (Afonine et al., 2018), in accordance with our MS results. Straight filament structures were similarly refined into the cryo-EM map EMD-0260. Acetylation of lysines to generate Figure 4D was performed using a plugin (Warnecke et al., 2014) for PyMOL (Schrödinger, 2017). Interfacial surface areas were calculated using the PISA server (Krissinel and Henrick, 2007).

Mass Spectrometry Analysis

Insoluble protein fractions (P3) were resuspended in 8 M urea buffer and digested overnight with endopeptidase LysC and trypsin at a 1:10 protease:substrate ratio as previously described (Higginbotham et al., 2019). Peptide samples were resuspended in loading buffer (0.1% (v/v) formic acid, 0.03% (v/v) trifluoroacetic acid and 1% (v/v) acetonitrile) and loaded onto a 20-cm column (internal diameter, 75 μm) packed with Reprosil-Pur 120 C18-AQ 1.9-μm beads (Dr. Maisch) and eluted over a 2-h 1%–50% buffer B reverse-phase gradient (buffer A, 0.1% (v/v) formic acid and 1% (v/v) acetonitrile in water; buffer B, 0.1% (v/v) formic acid in acetonitrile) generated by an Easy nLC UPLC system (Thermo). Peptides were ionized with 2.4-kV electrospray ionization voltage from a nano-ESI source (Thermo) on an Orbitrap Fusion Lumos mass spectrometer (Thermo). For samples analyzed in high resolution MS1 and MS2 scans, data-dependent acquisition of MS1 spectra were collected at 120,000 resolution (FWHM), and MS/MS spectra were collected in the Orbitrap at 15,000 resolution (FWHM) after higher energy dissociation (HCD) and/or electron-transfer dissociation (ETD) in a decision tree method (Swaney et al., 2008) or ETD supplemental activation with high energy (EThcD). For the first CBD case (CBD1) two MS runs were performed. The first with EThcD and HCD decision tree (CBD1_a), whereas a second run utilized ETD and HCD decision tree (CBD1_b) for MS/MS analyses. The second CBD case (CBD2_a) was analyzed using only EThcD and HCD decision tree for MS/MS analyses. The AD case (AD1) was analyzed with EThcD and HCD decision tree for MS/MS (AD1_a). A second analysis was also performed with ETD and HCD decision tree (AD1_b) for MS/MS analyses in which the product ions were detected in the ion trap. Raw data was deposited on ProteomeXchange (Project Accession # PXD016862). LC-MS/MS of sarkosyl-insoluble fractions from two pools of CBD (3 cases each pool) was performed on an Orbitrap-XL mass spectrometer as previously described (Bai et al., 2013) and raw data downloaded from www.synapse.org/#!Synapse:syn2397898

To identify tau peptides, Proteome Discoverer 2.3 was used to search and match MS/MS spectra to the human proteome database downloaded August 2019 from UniProt containing both Swissprot and TrEMBL entries (96,069 target entries) with a ± 10-ppm mass-accuracy threshold on the precursor. A maximum of 2 missed cleavages was set in the search, with variable modifications including phosphorylation (S/T/Y, +79.9663 Da), lysine ubiquitination (K, +114.0429 Da), acetylation (N-term/K, +42.420106 Da), arginine and lysine mono-/di-methylation (R/K, +14.0157/28.0313 Da), and methionine oxidation (M, +15.9949 Da). Fixed modifications included carbamidomethylation on cysteine (C, +57.0215 Da). A separate search was performed to map lysine mono-/di-/tri-methylation (K, +14.0157/28.0313/42.046950 Da) sites with a product ion mass tolerance of 0.02 Da. No tri-methylated lysine peptides were identified on tau. Thus, lysine tri-methylation was not included in the global PTM search on the same raw files in which the product ion mass tolerance was set to 0.05 Da for MS/MS data collected at high resolution. For AD1_b, the product ion mass tolerance was set to 0.6 Da for MS/MS data collected at low resolution in the ion-trap. Data from the CBD pools were searched with the same dynamic and fixed modifications described above with a ± 50-ppm mass-accuracy threshold on the precursor ion and product ion mass tolerance set at 0.6 Da for MS/MS data collected in the ion-trap. Percolator was used to filter the peptide spectral matches (PSM) in each sample to a false discovery rate (FDR) of < 1%. All MS/MS spectra for putative Tau PTMs were manually inspected. The mass spectrometry proteomics data generated in this study have been deposited to the ProteomeXchange Consortium via the PRIDE partner repository (Perez-Riverol et al., 2019) with the dataset identifier PXD016862.

Prediction of aggregation propensity

To approximate the effects of the acetylation of lysine residues in 4-repeat tau, we calculated its solubility before and after employing the K → Q mimic (Kamieniarz and Schneider, 2009) using the CamSol method (Sormanni et al., 2015).

QUANTIFICATION AND STATISTICAL ANALYSIS

The 0.143 Fourier Shell Correlation (FSC) criterion was used to estimate resolution of cryo-EM density maps.

DATA AND CODE AVAILABILITY

The cryo-EM maps have been deposited to the Electron Microscopy Data Bank (EMDB; https://www.ebi.ac.uk/pdbe/emdb/): accession numbers EMD-21200 for CBD doublet; EMD-21201 for CBD singlet; EMD-21207 for AD paired helical filament. The refined atomic models of the CBD fibrils and the AD paired helical filament have been deposited to the Protein Data Bank (PDB; https://www.rcsb.org/): accession numbers PDB: 6VH7 for CBD doublet fibril; PDB: 6VHA for CBD singlet fibril; PDB: 6VHL for AD paired helical filament; PDB: 6VI3 for straight filament. The raw mass spectrometry data has been deposited to the ProteomeXchange, www.proteomexchange.org/: PXD016862.

Supplemental Figures

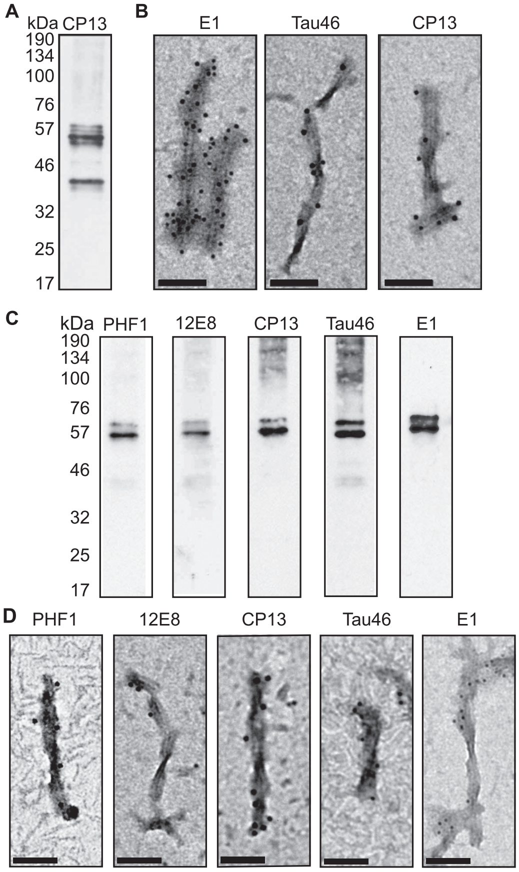

Figure S1. Characterization of Tau Fibrils from CBD Brain Used for Cryo-EM and MS, Related to Figure 1

(A) Western blot analysis of CP13 (pS202) immunoreactivity in sarkosyl-insoluble material (P3 fraction, see STAR Methods) from CBD case 1 brain tissue (frontal cortex).

(B) Labeling of sarkosyl-insoluble CBD tau filaments from CBD case 1 brain tissue (frontal cortex) revealed by immuno-electron microscopy with tau antibodies E1 (aa19–33), Tau46 (aa404–441), and CP13 (pS202), visualized with secondary antibody conjugated with 6 nm gold particle. Scale bar: 100 nm.

(C) Sarkosyl-insoluble material from CBD case 2 brain tissue (frontal cortex) used for additional MS analysis was evaluated by western blot, including the tau antibodies PHF1 (pS396/404), 12E8 (pS262, pS356), CP13 (pS202), Tau46 (aa404–441), and E1 (aa19–33).

(D) Representative immuno-electron microscopy images of sarkosyl-insoluble tau filaments purified from CBD case 2 brain tissue and stained with tau phosphor-specific antibodies PHF1 and 12E8, as well as tau antibodies CP13 (pS202), Tau46 (aa404-441), and E1 (aa19-33), visualized with secondary antibody conjugated with 6 nm gold particle. Scale bar: 100 nm.

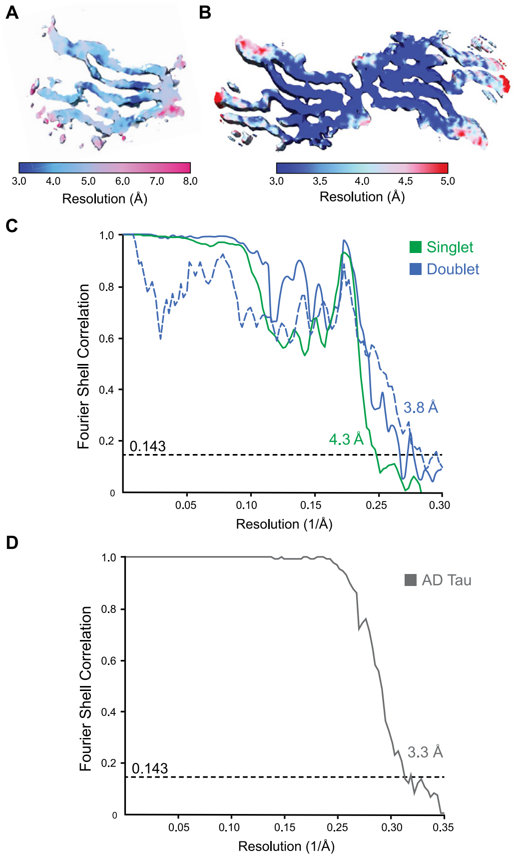

Figure S2. Resolution of Cryo-EM Singlet and Doublet Fibril Maps in CBD, Related to Figure 2

(A–C) Local resolution estimates for (A) singlet and (B) doublet fibrils. (C) Fourier shell correlation (FSC) curves between two independently refined half-maps for the singlet (green, solid) and doublet (blue, solid) fibrils in CBD. FSC curve between the cryo-EM reconstructions and the refined atomic model of the doublet fibril is shown as a dashed blue line. Because the resolution of the cryo-EM reconstruction of the singlet fibril is 4.3 Å, one protofilament of the doublet atomic model was rigid-body fitted into this map.

(D) FSC curve between two independently refined half-maps for the paired helical filament in AD (gray, solid).

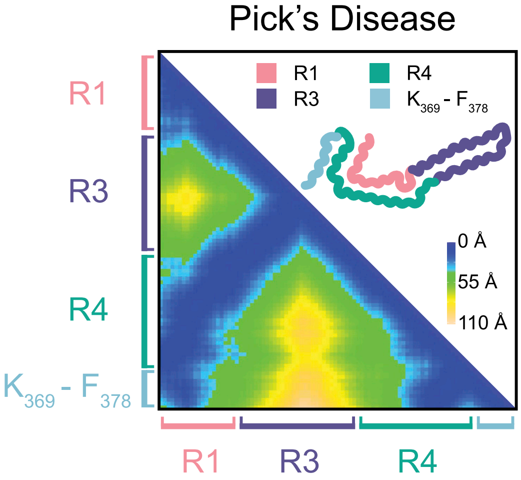

Figure S3. Intra-protofilament Contacts within Tau Protofilaments Found in Pick's Disease, Related to Figure 4

Heatmaps of inter-residue Cα-Cα distances within the tau protofilaments found in PiD, indicating the interactions between microtubule binding repeats (R1–R4) and $K_{369–378}$ of tau.

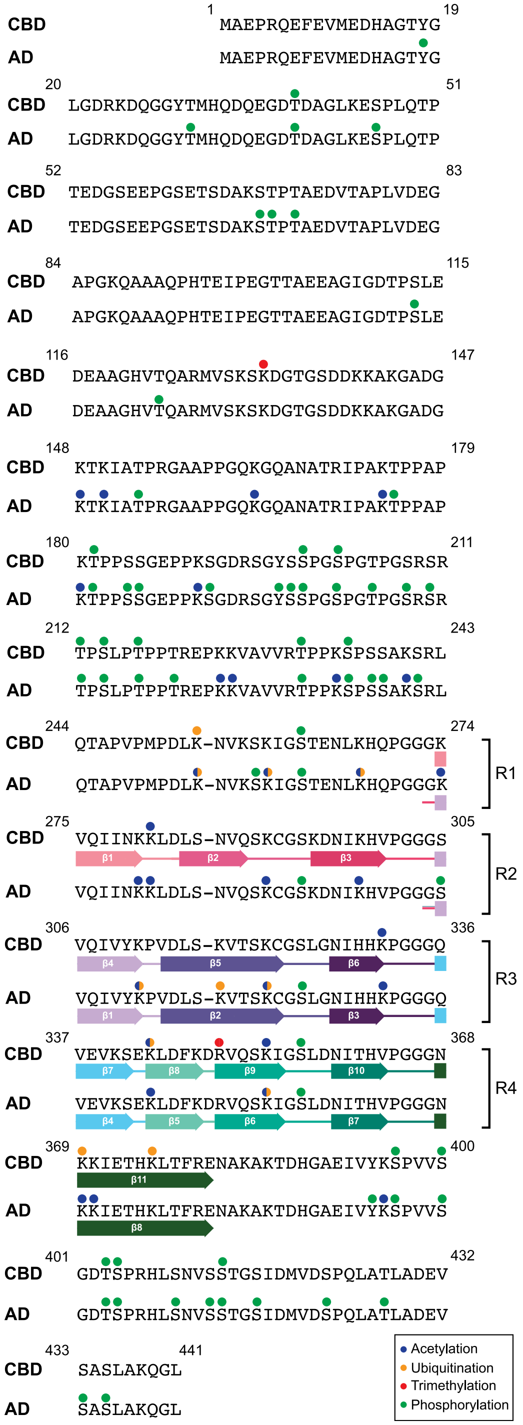

Figure S4. MS of Tau in CBD and AD Showing PTMs of the 2N4R Isoform, Related to Figure 3

Acetylation, ubiquitination, trimethylation, and phosphorylation sites are marked with blue, orange, red, and green balls, respectively. Additional PTMs of tau fibrils from AD patients' brains from the literature (Park et al., 2018) are also included and listed in Table S3.

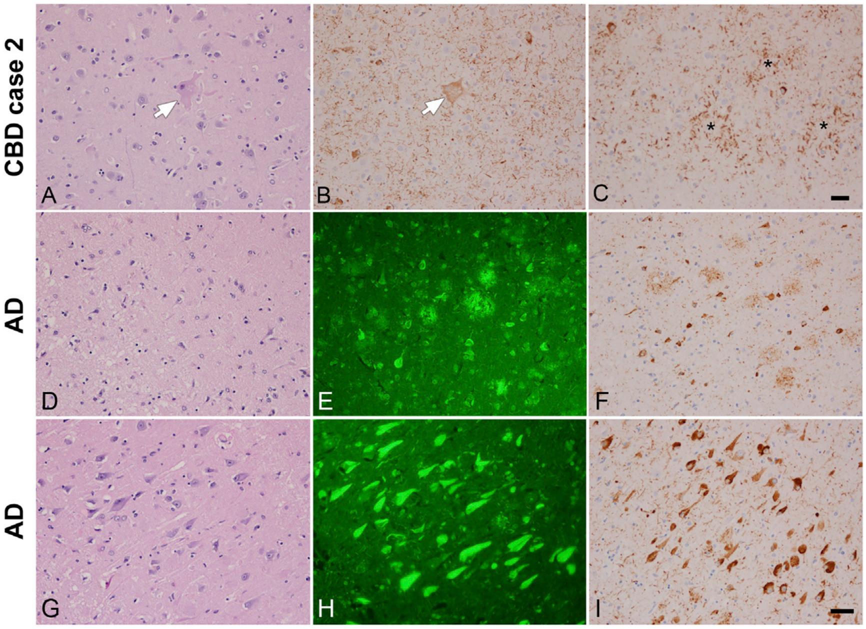

Figure S5. Light Microscopy of Tissue Sections from CBD Case 2 and AD Case, Related to Figure 1

(A–C) Tau immunohistochemistry showed neuronal and glial tauopathy consistent with cortical basal degeneration, including ballooned cortical neurons, many neuropil threads, pleomorphic small neuronal inclusions, and ballooned neurons in the limbic and frontal lobes. Scale bar: 20 μm.

(D–I) Neuropathological changes in the cortex and hippocampus of a patient with AD. Neurodegenerative changes revealed by (D and G) H&E staining, (E and H) thioflavin S, and (F and I) immunolabeling with PHF1 in (D–F) cortex and (G–I) hippocampus of the AD case used for cryo-EM and MS analysis. Scale bar: 50 μm.

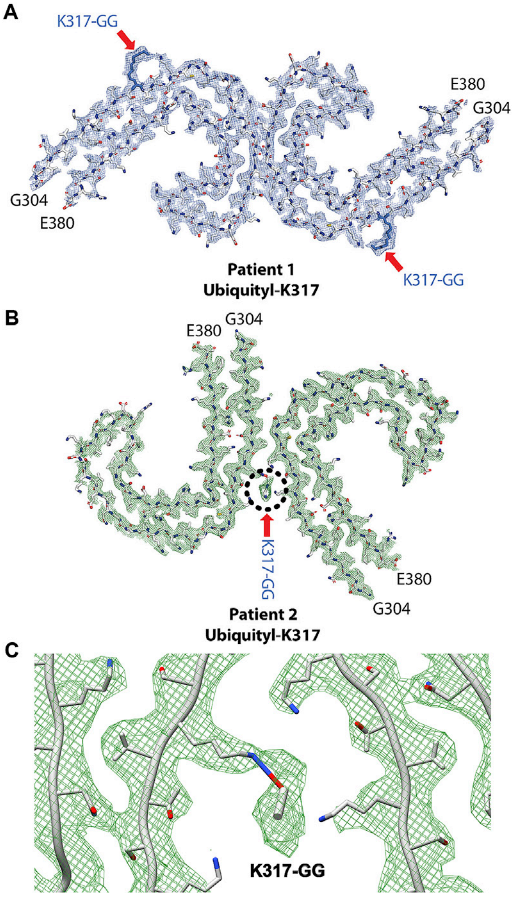

Figure S6. Ubiquitination of Filaments in the AD Tau Fold, Related to Figure 6

Cryo-EM cross-sectional density maps of (A) paired helical filament (this work, blue mesh) and (B) straight tau filaments (EMD-0260, green mesh) isolated from AD brains, with a covalently attached C-terminal $_{76}$GG$_{75}$ ubiquitin fragment built in to the atomic models at K$_{317}$. (C) Magnified view of inter-protofilament interface circled in (B) formed by packing between residues S$_{316}$–K$_{321}$ on each protofilament and mediated by a covalently attached C-terminal $_{76}$GG$_{75}$ ubiquitin fragment built in to the atomic model at K$_{317}$.

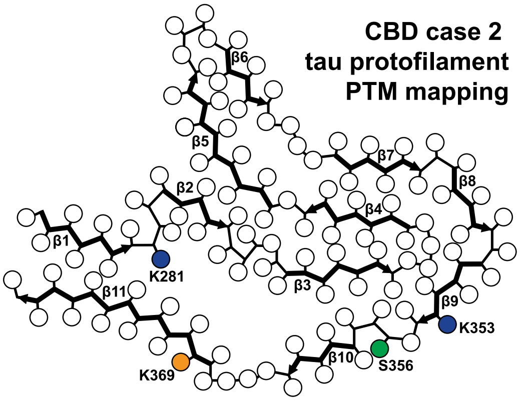

Figure S7. Schematic of PTMs in CBD Case 2, Related to Figure 3

PTMs detected by MS of tau filaments in CBD case 2 are mapped onto a schematic of the protofilament structure with acetylation, ubiquitination, trimethylation, and phosphorylation sites marked with blue, orange, red, and green balls, respectively.